

A new iron-based sulfate cathode material for high-performance potassium-ion battery

Xinyue Xu¹, Guodong Li², Hao Zhang¹, Nan Wang², Tinghang Xu¹, Hui Yang¹, Jie Xu³, Baofeng Wang¹, Junxi Zhang¹(™), Zhaolu Liu¹.²(™), Yongjie Cao¹.²(™)

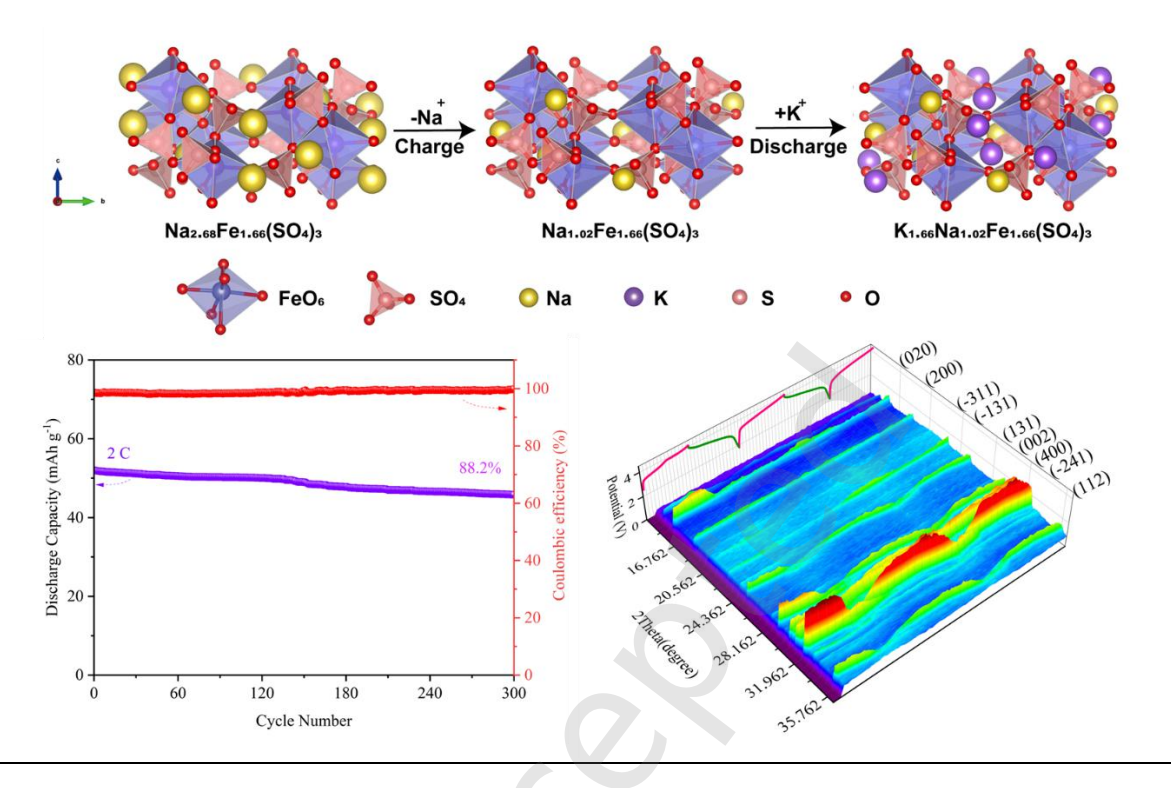
- ¹ Shanghai Key Laboratory of Materials Protection and Advanced Materials in Electric Power, Shanghai University of Electric Power, Shanghai 200090, China
- ² Department of Chemistry and Shanghai Key Laboratory of Molecular Catalysis and Innovative Materials, Fudan University, Shanghai 200433, China
- ³ School of Materials Science and Engineering, Anhui University of Technology, Ma'anshan 243002, China

Nano Res., Just Accepted Manuscript • https://doi.org/10.26599/NR.2025.94908121 https://www.sciopen.com/journal/1998-0124 on Sep. 27, 2025

© The Authors(s)

Just Accepted

This is a "Just Accepted" manuscript, which has been examined by the peer-review process and has been accepted for publication. A "Just Accepted" manuscript is published online shortly after its acceptance, which is prior to technical editing and formatting and author proofing. Tsinghua University Press (TUP) provides "Just Accepted" as an optional and free service which allows authors to make their results available to the research community as soon as possible after acceptance. After a manuscript has been technically edited and formatted, and the page proofs have been corrected, it will be removed from the "Just Accepted" web site and published officially with volume and article number (e.g., Nano Research, 2025, 18, 94906990). Please note that technical editing may introduce minor changes to the manuscript text and/or graphics which may affect the content, and all legal disclaimers that apply to the journal pertain. In no event shall TUP be held responsible for errors or consequences arising from the use of any information contained in these "Just Accepted" manuscripts. To cite this anuscript please use its Digital Object Identifier (DOI®), which is identical for all formats of publication.



This study reports the first fabrication of a novel alluaudite-type iron-based sulfate cathode material, potassium sodium iron sulfate $(K_{1.66}Na_{1.02}Fe_{1.66}(SO_4)_3$, denoted KNFS), via electrochemical ion exchange for potassium-ion batteries (PIBs), demonstrating remarkable electrochemical performance.



A new iron-based sulfate cathode material for high-performance potassium-ion battery

Xinyue Xu¹, Guodong Li², Hao Zhang¹, Nan Wang², Tinghang Xu¹, Hui Yang¹, Jie Xu³, Baofeng Wang¹, Junxi Zhang¹ Zhaolu Liu¹.2 , and Yongjie Cao 1.2 , and Yongjie Cao 1.2 , and Yongjie Cao 1.2 .

Received: 20 August 2025; Revised: 12 September 2025; Accepted: 27 September 2025

Address correspondence to Yongjie Cao, yongjie_cao@fudan.edu.cn; Junxi Zhang, <u>zhangjunxi@shiep.edu.cn</u>; Zhaolu Liu, 24113010007@m.fudan.edu.cn



Cite this article: Nano Research, 2025, 18, 94908121. https://doi.org/10.26599/NR.2025.94908121

ABSTRACT: Iron-based sulfates have emerged as promising cathode materials for potassium-ion batteries due to its low cost, high working potential, and environmentally friendly. However, the relatively large ionic radius and sluggish diffusion coefficient of K-ion pose significant challenges to the electrochemical performance and structural stability of cathode materials in PIBs. In this work, we successfully synthesis a new iron-based sulfate cathode material, potassium sodium iron sulfate (K_{1.66}Na_{1.02}Fe_{1.66}(SO₄)₃, KNFS), through an electrochemical ion exchange method. As a cathode material, it exhibits a reversible specific capacity of 83 mAh g⁻¹ and an average working potential of 3.84 V (vs. K/K⁺) at 0.1 C in PIBs. Even at 2 C, it still demonstrates a reversible specific capacity of 52 mAh g⁻¹ with a capacity retention ratio of 88.2 % after 300 cycles. The *in-situ* X-ray diffraction (XRD) and ex-situ X-ray absorption spectroscopy reveal that the K-ion storage mechanism in KNFS is predominantly governed by the reversible Fe³⁺/Fe²⁺ redox couple, which provides a theoretical specific capacity of 94 mAh g⁻¹ and involves minimal volume change (2.57 %). The first-principles calculations combined with XRD results indicate that the KNFS cathode exhibits a typical alluaudite-type crystal structure with multiple fast K-ion migration channels along the three-dimensional orientation.

KEYWORDS: energy storage, potassium-ion batteries, polyanion-type cathode materials, iron-based sulfate, high working potential

1 Introduction

The impending depletion of fossil fuels and the escalating environmental pollution have accelerated the development of renewable energy technologies. However, renewable energy sources such as wind and solar energy, which are influenced by natural conditions, exhibit characteristics of randomness, intermittency, and volatility, thereby hindering their effective utilization [1-3]. Consequently, development of sustainable energy storage systems has emerged as a focal point of global research efforts [4-11]. To date, electrochemical energy storage devices have been regarded as a promising candidate owing to their advantages in compact size, rapid response, high energy density, and long cycle life compared to other technologies such as pumped storage, compressed air energy storage, and flywheel energy storage. Among these the lithium-ion batteries (LIBs) have been widely adopted in markets such as small portable electronics and electric vehicles. Nevertheless, constrained by the limited crustal abundance and uneven global distribution of lithium, as well as current production capacities of LIBs, the technology is unable to

meet the surging global demand for large-scale energy storage (LSES) [12-18]. As a result, extensive research efforts have been directed toward developing low-cost energy storage systems as alternatives to LIBs for LSES [19, 20]. Potassium-ion batteries (PIBs) and sodium-ion batteries (SIBs) are considered promising alternatives in LSES due to their similar chemical properties to those of LIBs and more abundant elemental reserves compared to lithium [21-23]. Compared with SIBs, PIBs exhibit a higher working potential and can directly employ commercially available graphite as the anode material attributed to the lower standard redox potentials (-2.93 V vs. SHE for K/K+ and -2.71 V vs. SHE for Na/Na⁺) and smaller Stokes radii (1.84 Å for K-ion and 1.25 Å for Na-ion) [24-26]. However, the larger ionic radius of Kion (1.38 Å) compared to Li-ion (0.76 Å) and Na-ion (1.25 Å) results in electrode materials experiencing sluggish K-ion diffusion kinetics and poor structural stability [8, 27, 28]. Thus, the exploration works for a series of suitable cathode materials featuring larger K-ion diffusion channels and high structural stability is crucial for the development of PIBs [29-31]. Currently, cathode materials for PIBs are categorized into four primary categories: layered transition

¹ Shanghai Key Laboratory of Materials Protection and Advanced Materials in Electric Power, Shanghai University of Electric Power, Shanahai 200090. China

² Department of Chemistry and Shanghai Key Laboratory of Molecular Catalysis and Innovative Materials, Fudan University, Shanghai 200433, China

³ School of Materials Science and Engineering, Anhui University of Technology, Ma'anshan 243002, China

metal oxides [32, 33], Prussian blue analogues (PBAs) [34, 35], organic polycyclic materials [36, 37], and polyanionic compounds [38-42]. Among these, polyanion-type ironbased sulfate cathode materials have attracted significant research interest owing to their environmental friendliness. low cost, high working potential and excellent structural stability [43, 44]. The alluaudite-type sodium iron sulfate (Na₂Fe₂(SO₄)₃) is considered an ideal cathode material due to its high operating voltage (3.8 V), large theoretical specific capacity (120 mAh g⁻¹), and stable crystal structure [45, 46]. However, impurity phases such as FeSO₄ and Na₆Fe(SO₄)₄ are prone to form during synthesis and are difficult to eliminate completely. These impurities hinder the diffusion of Na-ions within the crystal structure, significantly impairing the reversible capacity and rate capability of the material. Therefore, it is essential to explore synthetic routes for obtaining pure-phase framework structures to achieve efficient sodium storage. Rojo et al. reported a nonstoichiometric sodium iron sulfate compound, $Na_{2.5}Fe_{1.75}(SO_4)_3/Ketjen/rGO$, which exhibits excellent capacity and rate performance, yet suffers from poor cycling stability [47]. Similarly, Cao et al. employed a spray-drying strategy to fabricate graphene-coated Na_{2.4}Fe_{1.8}(SO₄)₃ nanoparticles embedded within a three-dimensional graphene microsphere network. Despite the innovative design, this material also demonstrates unsatisfactory cycling performance [48]. Cao et al. reported that the alluaudite-type Na₈Fe₅(SO₄)₉@rGO material exhibits outstanding electrochemical performance, including a high operating voltage of 3.8 V (vs. Na/Na⁺), high reversible capacity at 0.2 C, excellent rate capability, and ultralong cycling stability [49]. Based on the advantages of sodium iron sulfate, it was employed as a cathode material for potassium-ion batteries. However, the alluaudite-type potassium ferric sulfate (K₂Fe₂(SO₄)₃, denoted as KFS) cannot be synthesized via conventional methods. The stable langeinite-type KFS can be directly synthesized through a solid-state reaction, however, it exhibits electrochemically inactive behavior [50-53]. Electrochemical ion exchange is an advanced technique for material synthesis modification, offering multiple significant advantages. Kim et al. first employed electrochemical ion exchange to prepare K₄Fe₃(PO₄)₂(P₂O₇) as a cathode material for potassium-ion batteries. This material exhibited a specific discharge capacity close to the theoretical value at C/20 and retained 70 % of its capacity even at a high rate of 5 C, demonstrating excellent electrochemical performance [54]. Similarly, Ruan et al. successfully synthesized Na_{4-x}K_xFe₃(PO₄)₂(P₂O₇)@rGO composites via a related ion exchange approach, confirming their feasibility for potassium-ion battery applications [55]. Zhang et al. also prepared K₃NaFe₃(PO₄)₂(P₂O₇) using an ion exchange strategy; the material exhibited high reversible specific capacity and excellent cycling stability at room temperature, along with superior performance compared to NFPP at low temperatures down to -40 °C [25].

In this work, multi-walled carbon nanotube (denoted as MCNTs)-modified off-stoichiometric pure-phase alluaudite-type $Na_{2.68}Fe_{1.66}(SO_4)_3$ (designated as NFS) was employed as a precursor to synthesize the alluaudite-type $(K_{1.66}Na_{1.02}Fe_{1.66}(SO_4)_3$, denoted as KNFS) material via an electrochemical ion-exchange method. As cathode material for PIBs, the KNFS exhibited a reversible specific capacity of 83 mAh g^{-1} with an average operating voltage of 3.84 V (vs. K/K^+) at 0.1 C. When tested at 2 C, it retained a reversible specific capacity of 52 mAh g^{-1} and demonstrated a capacity retention ratio of 88.2 % after 300 cycles. Based on

calculation results, the KNFS a cathode material can achieve a maximum energy and power density of 319 Wh kg⁻¹ and 1595 W kg⁻¹, respectively in PIBs. The K-ion storage mechanism of KNFS cathode in PIBs was investigated via *insitu* X-ray diffraction (XRD) and *ex-situ* X-ray absorption spectroscopy (XAS). The crystal structure, K-ion diffusion pathways and migration energies were elucidated through XRD refinement and first-principles calculations. These results demonstrate that the KNFS cathode exhibited excellent electrochemical performance, including a high energy density, low cost and excellent cycling stability in PIBs, indicating its potential as a promising cathode material for future LSES.

2 Results and Discussion

The Retrieved-refined XRD pattern of NFS was shown in **Figure S1**, which showed a pure phase structure without any crystalline impure phase. The Figure S2 presented the Fourier transform infrared (FTIR) spectrum of NFS. The characteristic peaks located at 1077 cm⁻¹, 986 cm⁻¹, and 624 cm⁻¹ were corresponded to the asymmetric stretching vibration, symmetric stretching vibration, and asymmetric bending vibration of the SO₄²⁻ group, respectively, which aligned with the reported infrared spectral ranges of typical sulfates [56], confirming the structural integrity of the sulfate moiety. Additionally, the absorption peak at 594 cm⁻¹ could be attributed to the skeletal vibration mode of isolated FeO₆ octahedron. Additionally, the Raman spectrum of NFS@MCNTs was shown in Figure S3. The characteristic peaks at 650 cm⁻¹ and 1010 cm⁻¹ were assigned to the bending vibration and symmetric stretching vibration of SO₄²-, respectively. The characteristic peaks at 1360 cm⁻¹ and 1590 cm⁻¹ corresponded to the disordered carbon structure (D band) and graphitized carbon (G band), respectively, confirming the successful introduction of MCNTs. The ID/IG ratio of the NFS@MCNTs composite was 0.87, indicating its remarkable electrical conductivity. The electrochemical performance of the NFS cathode material in SIBs was evaluated using CR-2016 coin cells. The galvanostatic charge/discharge cycling of NFS cathode in SIBs was performed within a voltage window of 2.0-4.3 V (vs. Na/Na⁺). As shown in **Figure S4a**, the voltage profiles of the NFS cathode recorded at 0.1 C exhibited an initial charge specific capacity of 100 mAh g-1 with an average nominal working potential of 3.8 V (vs. Na/Na⁺) and the Coulombic efficiency was 94%. The presence of multiple plateaus correlated with Na-ion insertion into different sodium occupancy sites [48, 57]. The corresponding cyclic voltammetry (CV) curves (inset of Figure S4a) revealed three pairs of oxidation/reduction peaks associated with the redox of Fe³⁺/Fe²⁺ in NFS, along with three distinct plateau regions observed at 4.05, 3.83, and 3.48 V. The NFS cathode also demonstrated superior rate capability, achieving desirable cycling stability across various current rate and retaining 60 mAh g-1 even at a high current density of 30 C (Figure S4b). Furthermore, the NFS cathode exhibited exceptional cycling durability, with capacity retention rates of 96.7 % and 95.6 % after 300 cycles at 1 C and 2 C, respectively (Figure S4c). The diffusion coefficients of NFS during continuous sodium insertion/extraction were observed to range from 1.79×10⁻¹¹ to 1.99×10⁻¹⁰ cm² s⁻¹⁰ ¹ (Figure S4d). These results confirmed the outstanding

electrochemical performance of the NFS cathode material in SIBs. Building on the exceptional electrochemical properties of the NFS cathode material in SIBs, this study proposed a theoretical framework to extend the K_{2.68}Fe_{1.66}(SO₄)₃ (denoted as KFS) structural analog to PIBs, though initial attempts were unsuccessful. By leveraging the structuredirecting effect of pre-embedded Na-ions within the matrix, the controlled incorporation of K-ions into the iron-based sulfate framework was effectively realized through an electrochemical ion-exchange synthesis approach. This advancement enables the extension of this material system to the field of PIBs. As illustrated in Figure 1a, the NFS crystal structure exhibits the characteristic polyanionicframework alluaudite-type structure, in which Na-ions occupied three crystallographic sites (Na1, Na2, and Na3), while Fe-ions occupied two distinct crystallographic sites. Its octahedrally coordinated Fe sites (FeO₆) formed doubleoctahedral Fe₂O₁₀ dimer units through edge-sharing. These dimers were then connected via SO₄ tetrahedral units in a corner-sharing fashion, constituting a three-dimensional framework structure with large tunnels along the [001] direction [46]. After partial Na-ion extraction, the Na_{1.02}Fe_{1.66}(SO₄)₃ (denoted as Na_{1.02}FS) phase was formed. Upon K-ion insertion into Na_{1.02}FS, the KNFS phase emerged, exhibiting a larger unit cell volume compared to NFS due to the incorporation of the larger K-ion. Based on ICP analysis, the atomic ratio of K. Na. Fe. and S in the KNFS material was determined to be 1.66: 1.02: 1.66: 3. The corresponding mass fractions (wt%) of the elements are provided in Figure S5. The charge/discharge curves of the electrochemical ionexchange process were shown in Figure 1b, which demonstrated that during charging, Fe²⁺ was oxidized to Fe³⁺ accompanied by partial Na-ion extraction, resulting in an

open framework Na_{2.68-x}Fe_{1.66}(SO₄). A half-cell was assembled using Na_{1.02}FS as the cathode, 0.8 mol L⁻¹ KPF₆ dissolved in Ethylene Carbonate/Propylene Carbonate (EC/PC, 1:1 by vol.) was employed as the electrolyte, and potassium metal as the anode. Upon discharging to 2 V, effective K-ion insertion was observed, completing the Na/K-ion exchange to form the PIBs cathode material KNFS, which subsequently served as a K-ion host during cycling. The initial charge/discharge specific capacity was tested at 9.4 mA g⁻¹ within a voltage window of 2.0-4.3 V. The XRD analysis was employed to characterize the structural evolution during Na/K-ion exchange process. As shown in Figure 1c, after Na-ion extraction, the lattice spacing decreased, and according to Bragg's law, the diffraction peak shifted to the right by 0.18°. During the discharge process, the insertion of the larger Kion into Na-ion sites caused framework expansion, leading to increased lattice spacing with diffraction peaks shifting to the left ($\Delta 2\theta = 0.30^{\circ}$). Conversely, K-ion extraction induced a rightward shift of diffraction peaks. The phase purity and structural integrity of KNFS were confirmed through Rietveld refinement of the full-pattern XRD data (Figure 1d). KNFS crystallized in the C2/c space group without detectable impurities or secondary phases. The refined lattice parameters (a = 13.1401 Å, b = 13.0138 Å, c = 6.5379Å) and reliability factors (Rp = 5.64 %, Rwp = 7.78 %, R_B=0.91 %) confirmed the phase purity of the cathode material. Figure 1e showed the refined crystal structure of KNFS. Despite sharing the same crystal structure as NFS, KNFS exhibited distinct lattice parameters due to ion exchange between the larger K-ion (1.38 Å) and the smaller Na-ion (1.02 Å) (Supporting Information Table S1). Detailed crystal parameters for NFS and KNFS were provided in **Supporting Table S2 and S3**, respectively.

Nano Research | Vol. XX, No. XX

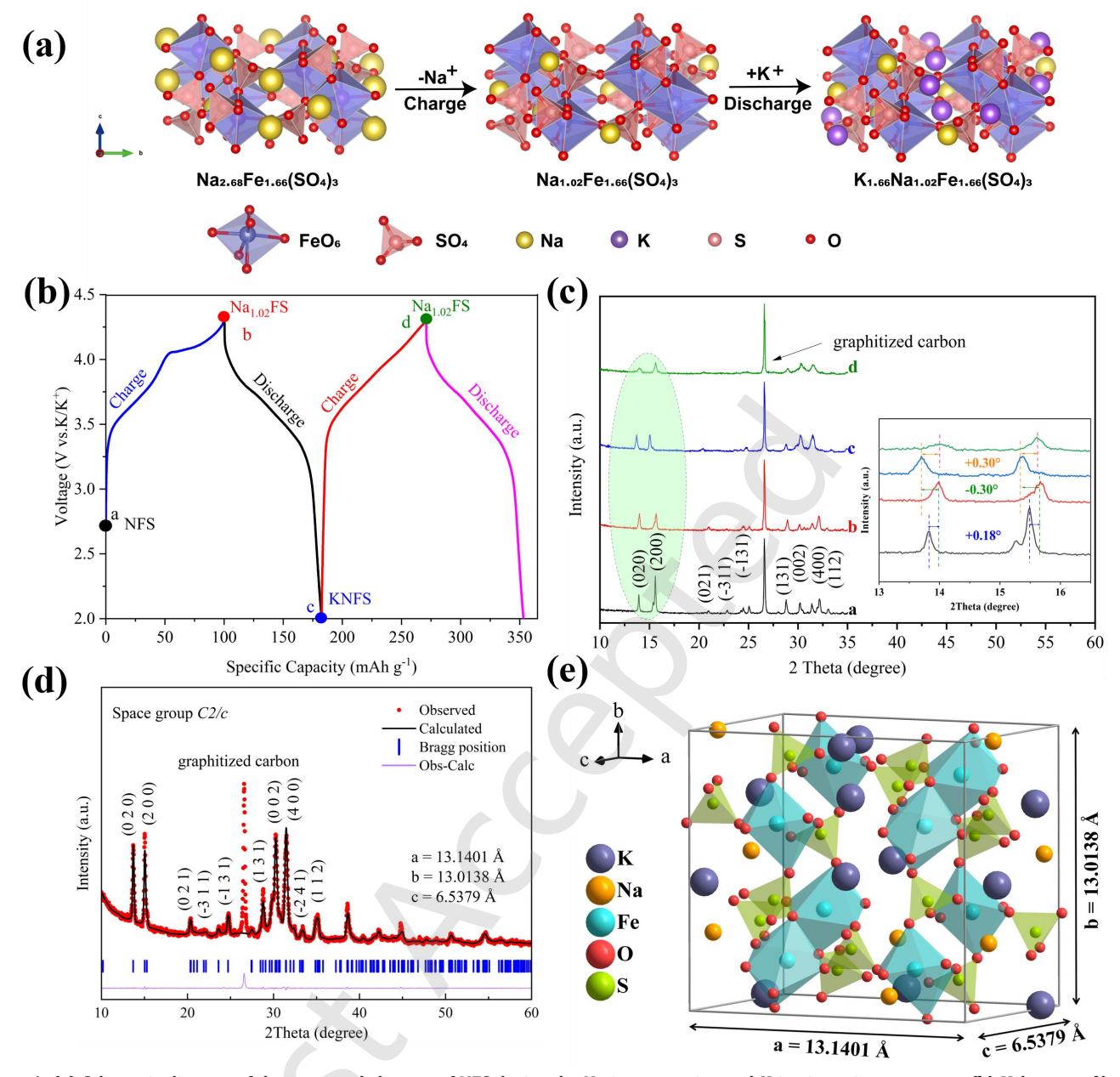


Figure 1. (a) Schematic diagram of the structural changes of NFS during the Na-ion extraction and K-ion insertion processes; **(b)** Voltage profiles of NFS during desodiation and subsequent potassiation/depotassiation; **(c)** XRD patterns collected at different stages marked in Figure (b); **(d)** Rietveld-refined XRD pattern of KNFS; **(e)** Refined crystal structural model of KNFS.

The morphological and structural characteristics of NFS and KNFS electrode materials were systematically field-emission investigated using scanning electron microscopy (FE-SEM), high-resolution transmission electron microscopy (HR-TEM), and energy-dispersive spectroscopy (EDS) for elemental mapping. As shown in Figures 2a and 2d, both NFS and KNFS samples exhibited spherical secondary particles with diameters ranging from 10 to 20 μm. Corresponding HRTEM images (Figures 2b and **2e)** exhibited well-defined lattice fringes in both samples with interplanar spacings of 0.32 nm and 0.39 nm, respectively, which correspond to the (-202) and (-311) planes. Furthermore, the absence of surface carbon layers indicated that the 400 °C thermal treatment temperature was insufficient to achieve complete carbonization of citric acid. Consequently, MCNTs were additionally incorporated to fabricate the composite material. As revealed in the insets of Figures 2b and 2e, the MCNTs with an average diameter of

2-3 nm were tightly embedded within the crystal frameworks of both NFS and KNFS materials. This configuration can enhance the electronic conductivity and structural stability of the materials, facilitate rapid charge transfer, and alleviate mechanical stress during cycling. Elemental mapping analysis via EDS (Figures 2c and 2f) further confirmed the successful incorporation of K into KNFS, along with a homogeneous distribution of K, Na, Fe, S, and 0 elements. The evolution of Fe³⁺/Fe²⁺ valence states during the charge/discharge process provided direct evidence for understanding the redox mechanisms. As illustrated in Figure S7, ex-situ XPS was employed to analyze the Fe oxidation states and variations in Na and K content. In the pristine electrode, the Fe 2p spectrum displayed two peaks at 711.3 eV (Fe $2p_{3/2}$) and 724.8 eV (Fe $2p_{1/2}$), characteristic of Fe²⁺, along with a sharp Na 1s peak at 1071.8 eV and no detectable K signal. Upon charging to 4.3 V, the Fe 2p_{3/2} and Fe 2p_{1/2} binding energies shifted to higher values of 712.1 eV and 725.6 eV, respectively, corresponding to the oxidation of Fe^{2+} to Fe^{3+} . Concurrently, the Na 1s peak intensity decreased significantly, indicating Na-ion extraction and the formation of a desodiated framework, Na_{1.02}FS. When discharged to 2 V, the Fe $2p_{3/2}$ and Fe $2p_{1/2}$ binding energies reverted to 711.3 eV and 724.8 eV, confirming the reduction of Fe^{3+} to Fe^{2+} and demonstrating the reversible Fe^{3+}/Fe^{2+} redox process. Notably, the Na 1s peak intensity remained nearly unchanged, suggesting that residual Na-ion

do not participate in further electrochemical reactions. Two new peaks emerged at 293.2 eV (K $2p_{3/2}$) and 296.0 eV (K $2p_{1/2}$), confirming K-ion insertion into the polyanionic framework to form KNFS. The electrode exhibited a stable working voltage of approximately 3.84 V, driven by the Fe^{3+}/Fe^{2+} redox couple in the sulfate framework, with reversible ion insertion/extraction maintaining charge balance.

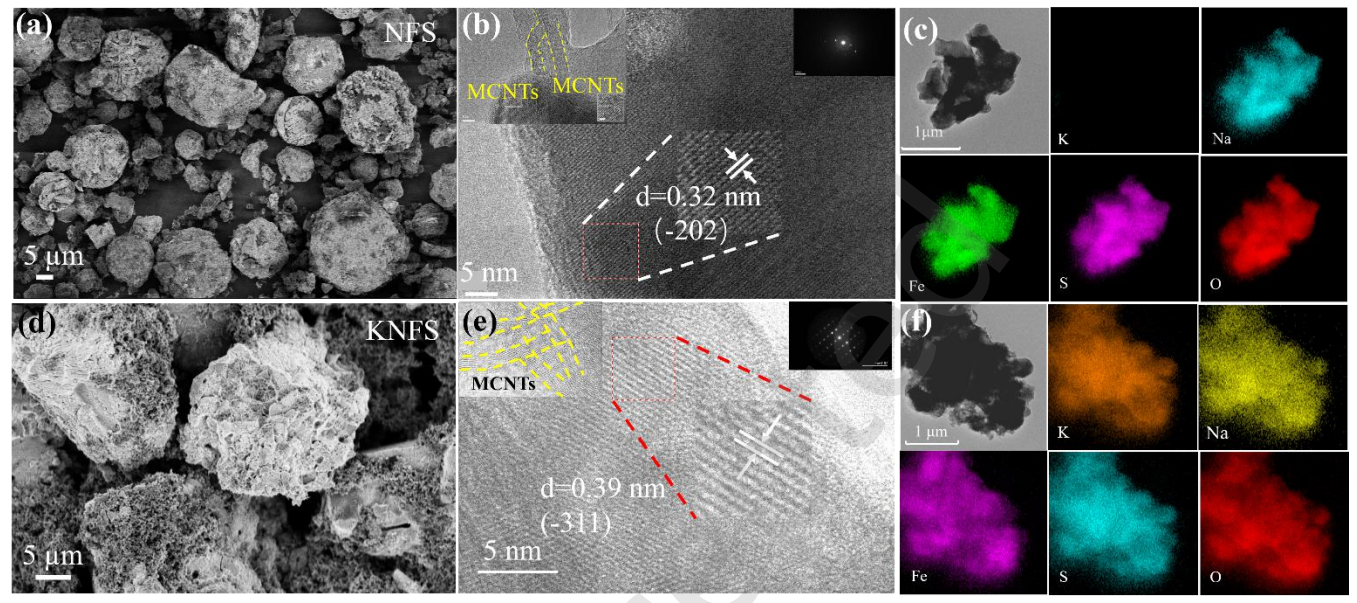


Figure 2. (a) SEM image of NFS; (b) HR-TEM image of the NFS (inset: SAED pattern); (c) Elemental mapping image of NFS; (d) SEM image of KNFS; (e) HR-TEM image of the KNFS (inset: SAED pattern); (f) Elemental mapping image of KNFS.

As shown in **Figure 3a**, the stable reversible capacity measured at 0.1 C was approximately 83 mAh g-1. Notably, when K-ion replaced Na-ion for insertion and extraction into the Na_{1.02}FS host, significant differences emerged in the voltage profiles. Although the Fe-based sulfate framework accommodated K-ion insertion, the larger ionic size induced structural rearrangement, resulting in a sloping voltage curve featuring a single Fe3+/Fe2+ redox plateau. The KNFS cathode delivered an average operating voltage of 3.84 V (vs. K/K+), which highlighted the enhanced "inductive effect" conferred by the SO₄²- polyanion in the crystal structure. The CV analysis of KNFS was conducted at a scan rate of 0.1 mV s⁻¹ ¹ (inset of Figure 3a). Broad cathodic and anodic peaks were observed in the CV curve of KNFS for PIBs. The absence of distinct voltage plateaus was attributed to the minimal potential gaps between successive redox steps. To further investigate rate capability, galvanostatic charge-discharge (GCD) tests were performed at varying current densities (Figure 3b). The KNFS cathode exhibited rate capacities of 77.0, 66.0, 57.2, 49.5, and 42.2 mAh g⁻¹ at 0.3, 0.5, 1, 3, and 5 C, respectively in PIBs. When the current density was restored to 0.3 C, the reversible specific capacity could recover to 76.3 mAh g⁻¹, demonstrating robust structural stability and excellent rate capability. Notably, KNFS cathode demonstrated exceptional long-term cycling stability, achieving specific capacity retention ratio of 83.6 % and 88.4 % after 300 cycles at 1 C and 2 C current densities, respectively with a near-unity Coulombic efficiency (~99 %) that underscored its high structural robustness and electrochemical reversibility (Figure 3c). The structural integrity of the polyanionic KNFS framework was pivotal for

reversible K-ion insertion/extraction over prolonged cycling. The capacity retention relied critically on the rigid framework's ability to buffer lattice strain during K-ion insertion/extraction, where the three-dimensional covalent network enabled adaptive synergy between K-ion migration pathways and lattice expansion. Additionally, the galvanostatic intermittent titration technique (GITT) was employed to determine K-ion diffusion coefficient. During the initial charging process, the GITT measurement involved alternating 10 min charging and 60 min relaxation intervals until the voltage reached 4.3 V (vs. K/K⁺). The same protocol was applied during discharge to 2 V. The K-ion diffusion coefficient ($D_{\rm K}^+$) was calculated using Equation (1):

$$D_{K^{+}} = \frac{4}{\pi \tau} \left(\frac{m_{\rm B} V_{\rm m}}{M_{\rm B} S} \right)^{2} \left(\frac{\Delta E_{\rm s}}{\Delta E_{\rm t}} \right)^{2}, (\tau \ll \frac{L^{2}}{D_{K^{+}}})$$
 (1)

where τ represents the pulse duration, m_B denotes the active mass, V_m stands the molar volume, M_B refers the molar mass, S indicates the electrode-electrolyte contact area, L signifies the electrode thickness, $\Delta E \tau$ corresponds to the voltage change during the pulse, and ΔEs reflects the relaxation voltage change. The GITT curve of KNFS was shown in Figure 3d, and the K-ion diffusion coefficient was determined to range from 1.29×10^{-11} to 2.01×10^{-10} cm² s⁻¹. The results demonstrated that the material exhibited superior K-ion transport kinetics. The electrochemical impedance spectroscopy (EIS) further confirmed the favorable kinetics of KNFS. The Nyquist plot (Figure S8) showed a small semicircle, indicating a low charge-transfer resistance (Rct \sim 100 Ω). The CV curves at scan rates ranging from 0.2 to 1.0 mV s⁻¹ (Figure 3e) showed increasing peak currents and minor peak potential shifts (approximately 230 mV) with elevated scan rates, signifying highly reversible redox reactions. The calculated kinetic parameter b-values (inset in Figure 3e), ranging from 0.6 to 0.9, indicated a mixed mechanism governed by diffusion-controlled and capacitive-controlled processes. According to the analysis of capacitive contributions at various scan rates (as shown in Figure S9), the KNFS electrode material was found to exhibit primarily battery-type energy storage behavior, which contributes to high energy density, along with a relatively significant pseudocapacitive behavior, thereby endowing the material with good rate capability. At a scan rate of 1 mV s⁻¹, the capacitive contribution reached 40 %, indicating that the nanoscale structure and surface characteristics of the material were optimized, enabling it to maintain high capacity while demonstrating faster response capabilities compared to conventional battery materials. (The detailed calculations utilizing Equations S1 and S2 can be found in the Supporting Information.). Based on calculations using Formulas S3 and S4, the KNFS cathode attained a high energy density of 319 Wh kg-1 and a high power density of 1595 W kg⁻¹ (**Figure 3f**), thereby demonstrating considerable promise for application as a next-generation high-performance PIB cathode.[38, 58-67] To investigate the low-temperature electrochemical performance of the KNFS material, charge-discharge tests were conducted at -40 °C. As shown in Figure S10a, the KNFS-based potassium-ion battery delivered a specific discharge capacity of 49.68 mAh g-1 at a current density of 0.1 C. Under the same conditions, the NFS exhibited a specific discharge capacity of 56.8 mAh g-1 (Figure S10c). Compared with its room-temperature performance, KNFS demonstrated a significantly lower capacity decay rate at low temperatures than the NFS material. As depicted in Figure S10b, the KNFS electrode maintained a capacity retention of 85.2 % after 500 cycles at 1 C, indicating good cycling stability. In contrast, the NFS cathode material showed poor cycling stability at -40 °C, with noticeable fluctuations in its capacity decay curve

within the first 80 cycles (Figure S10d). These results confirmed that **KNFS** possesses outstanding temperature performance and structural stability as a cathode material for PIBs. To further evaluate the practical application potential of the KNFS cathode material, an HC||KNFS full cell was assembled by pairing KNFS with a commercial hard carbon (HC) anode. Figure S11a illustrated the working mechanism of the full cell: during charging, Kions were extracted from the KNFS cathode and inserted into the HC anode; during discharging, K-ions were released from the HC anode and return to the cathode. The full cell was constructed using KNFS as the cathode and pre- potassiated HC as the anode (precycled twice in a half-cell), with an electrolyte of 0.8 M KPF₆ in a mixture of EC and PC (1:1 by volume). The negative-to-positive electrode capacity ratio was controlled at 1:1.05. Figure S11b displayed the normalized actual charge/discharge capacity of the assembled full cell at 0.1 C, which was measured to be 0.20 mAh, with an average operating voltage of 3.3 V. Figure S11c showed the rate performance of the full cell at different current densities of 0.1 C, 0.3 C, 0.5 C, 1 C, and 2 C. Figure presented the cycling performance at 1C, demonstrating a capacity retention of 95.5% after 100 cycles. To investigate the structural and morphological stability of the KNFS electrode material after long-term cycling, XRD, SEM, and EDS analyses were conducted. As shown in Figure **S12a.** the XRD pattern after cycling remained largely unchanged, indicating that the crystal structure of the electrode material maintained high stability throughout the prolonged cycling process. The SEM image in Figure S12b revealed no significant morphological changes in the KNFS electrode after cycling, with the material retaining its welldefined morphology, suggesting uniform strain distribution within the particles and demonstrating excellent structural stability. Furthermore, EDS elemental analysis confirmed that all elements remained homogeneously distributed (Figure S12c).

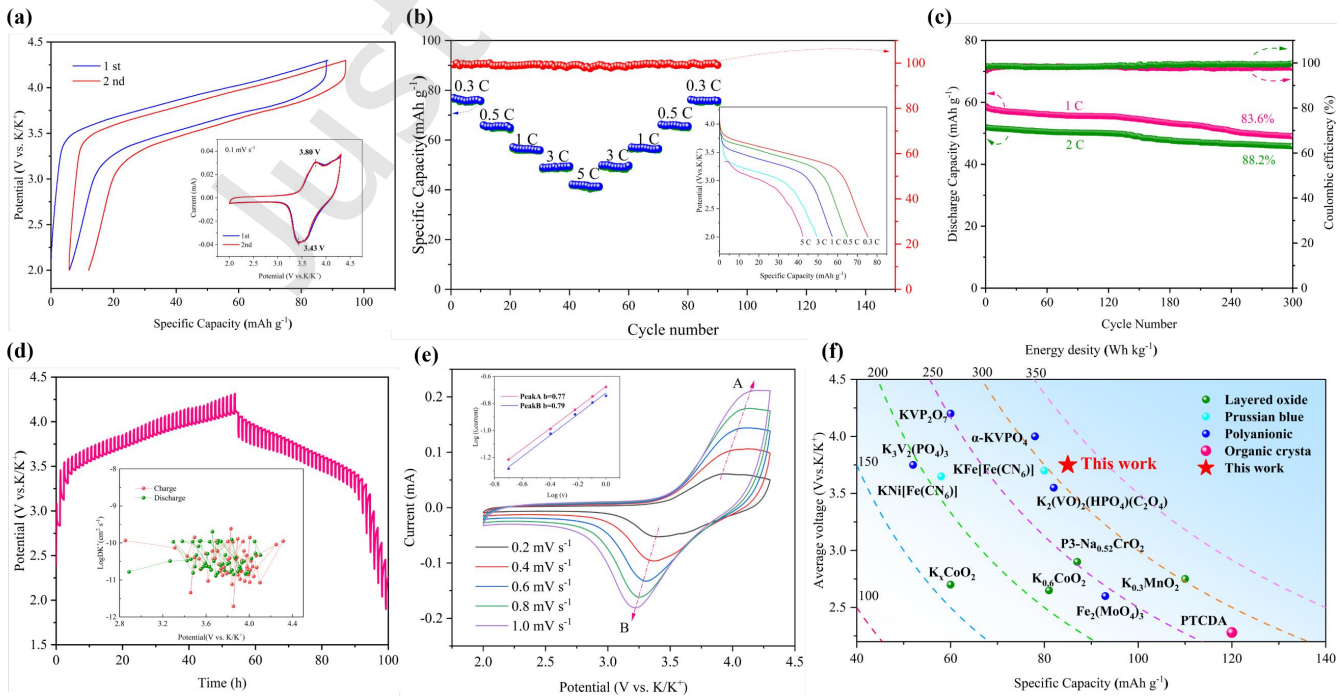


Figure 3. (a) Voltage profiles of KNFS in the initial two cycles. The inset shows the corresponding CV curves; (b) Rate capability of the material and its discharge profiles at various current rates; (c) Cycling stability of KNFS at 1 and 2 C; (d) GITT curves and K-ion diffusion coefficients of KNFS; (e) CV

curves of KNFS at different scan rates (inset: b-value calculation); (f) The capacity, voltage, and energy density of this cathode are competitive with those of reported PIB cathodes.

The in-situ XRD system was employed to systematically investigate the evolution of the crystal structure and the Kion storage mechanism of the KNFS electrode during the charge-discharge cycles. In the pristine state, all characteristic diffraction peaks of the electrode material were distinctly observed. As illustrated in Figure 4a, the diffraction peaks at 38.4° and 44.7° corresponded to the (111) and (200) planes of the aluminum (denoted as Al) current collector (PDF#00-004-0787) (all peak positions were calibrated based on the diffraction peaks of Al). In the initial state, the diffraction peaks at 14.23°, 15.64°, 22.88°, 25.29°, 28.98°, 30.46°, 31.20°, 32.34°, 35.34° and 42.67° were attributed to the (020), (200), (-311), (-131), (131), (002), (400), (-241), (112) and (222) planes of the NFS phase (PDF #97-025-2403) [56]. As shown in Figure 4b, the GCD profiles measured at a rate of 0.1 C within the voltage window of 2.0 to 4.3 V exhibit strong correlations with the contour plots. During the charge-discharge process, these diffraction peaks exhibited reversible shifts. To accurately determine the magnitude of these shifts, two-dimensional magnified contour plots of selected crystal planes were presented in Figure 4c. During the initial charging stage, the (020), (-131), (131), (-241) and (112) planes shifted to the right by 0.41°, 0.52°, 0.74°, 0.53°, and 0.62°, respectively, indicating the extraction of Na-ions and the formation of the Na_{1.02}FS phase, which resulted in unit cell contraction.

During the subsequent discharge process, the same set of crystal planes shifted to the left by 0.47°, 0.67°, 0.83°, 0.70° and 0.80°, respectively, confirming the insertion of K-ions into the Na-ion vacancies to form the KNFS phase, thereby causing significant expansion of the poly-anion framework. During the following charging cycle, the crystal planes shifted again to the right by 0.50°, 0.69°, 0.83°, 0.72° 0.79°, respectively, corresponding to the extraction of K-ions. Throughout the K-ion insertion and extraction processes, the positions of all characteristic diffraction peaks remained reversible, demonstrating the presence of a structurally stable K-ion storage mechanism within the material lattice. Figure 4d illustrated the evolution of lattice parameters calculated through Equation S5 from selected diffraction peaks during cycling. The lattice parameters displayed a contraction trend during the charging phase, as K-ions were progressively extracted, followed by reversible recovery during discharge, with an overall volume fluctuation of approximately 2.57 % per cycle (The detailed calculation process was described in the Supporting Information), significantly lower compared to other reported cathode materials for PIBs (Figure 4e) [54, 68-74]. This observation demonstrated that KNFS, as a cathode material for K-ion batteries, possessed minimal volumetric variation and exceptional structural stability.

Nano Research | Vol. XX, No. XX

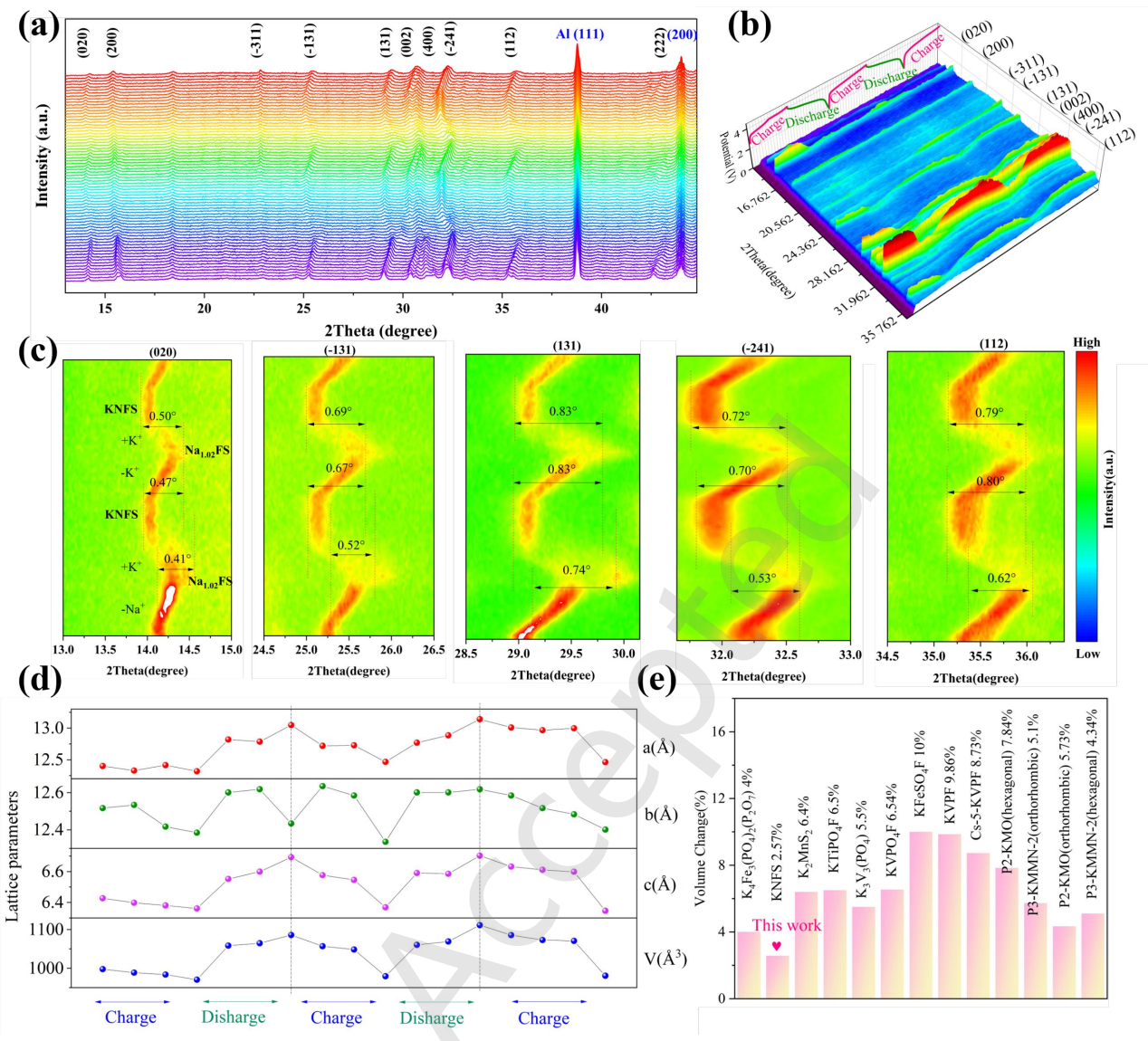


Figure 4. Characterization of the K-ion storage mechanism. **(a)** In-situ XRD patterns of KNFS; **(b)** Contour plot with corresponding GCD profiles; **(c)** Magnified view of selected diffraction peaks. **(d)** Corresponding variation in lattice parameters; **(e)** Volume changes in KNFS and other cathode materials for PIB.

To elucidate the charge compensation mechanism, exsitu X-ray absorption fine structure (XAFS) experiments were conducted to probe the detailed valence electronic structure of KNFS during the charge and discharge processes. As shown in **Figure 5a**, the labeled points a, b, c, d, and e on the GCD profile corresponded to specific states of charge (SOC) and their corresponding crystal structures: point a (pristine electrode, charged to 4.3 V), point b (discharged to 3.67 V), point c (discharged to 2 V), point d (charged to 3.74 V), and point e (charged to 4.3 V). At these designated SOC points, the local coordination environment and chemical states of Fe in the KNFS electrodes were characterized (Figure 5b). During the cycling process, the transition metal Fe exhibited reversible redox behavior. In the pristine electrode (desodiated state), the Fe K-edge absorption energy was observed at 7116 eV, which is characteristic of Fe³⁺. Upon discharge to 2 V (Figure 5c), a significant lowenergy shift of the Fe K-edge to 7112 eV was detected, indicating the reduction of Fe³⁺ to Fe²⁺. This change was accompanied by K-ions insertion, leading to the formation of KNFS. Conversely, upon charging to 4.3 V (Figure 5d), the

absorption edge energy returned to 7116 eV, signifying complete extraction of K-ions. Collectively, these findings confirm the reversible Fe3+/Fe2+ redox transition, which is consistent with the results of XPS analysis. Fouriertransform extended EXAFS analysis in R-space further revealed the structural evolution of the KNFS electrode at different states of charge (Figure 5e). During charging, as the state of charge (SOC) increased, the Fe-O bond length shortened from 1.66 Å to 1.41 Å due to Fe oxidation and enhanced Fe-O bond covalency. Conversely, during discharging, Fe reduction and weakened Fe-O bond covalency resulted in bond elongation from 1.41 Å to 1.66 Å, demonstrating reversible Fe-O bond adjustment during cycling. Additionally, wavelet transform (WT) analysis of Fe K-edge EXAFS oscillations was carried out, as shown in Figure 5f, to resolve the Fe coordination environment. The results confirmed that the Fe coordination configuration in KNFS corresponded to Fe-O bonding, with no evidence of phase separation or secondary coordination motifs within the detection limits.

Nano Research | Vol. XX, No. XX

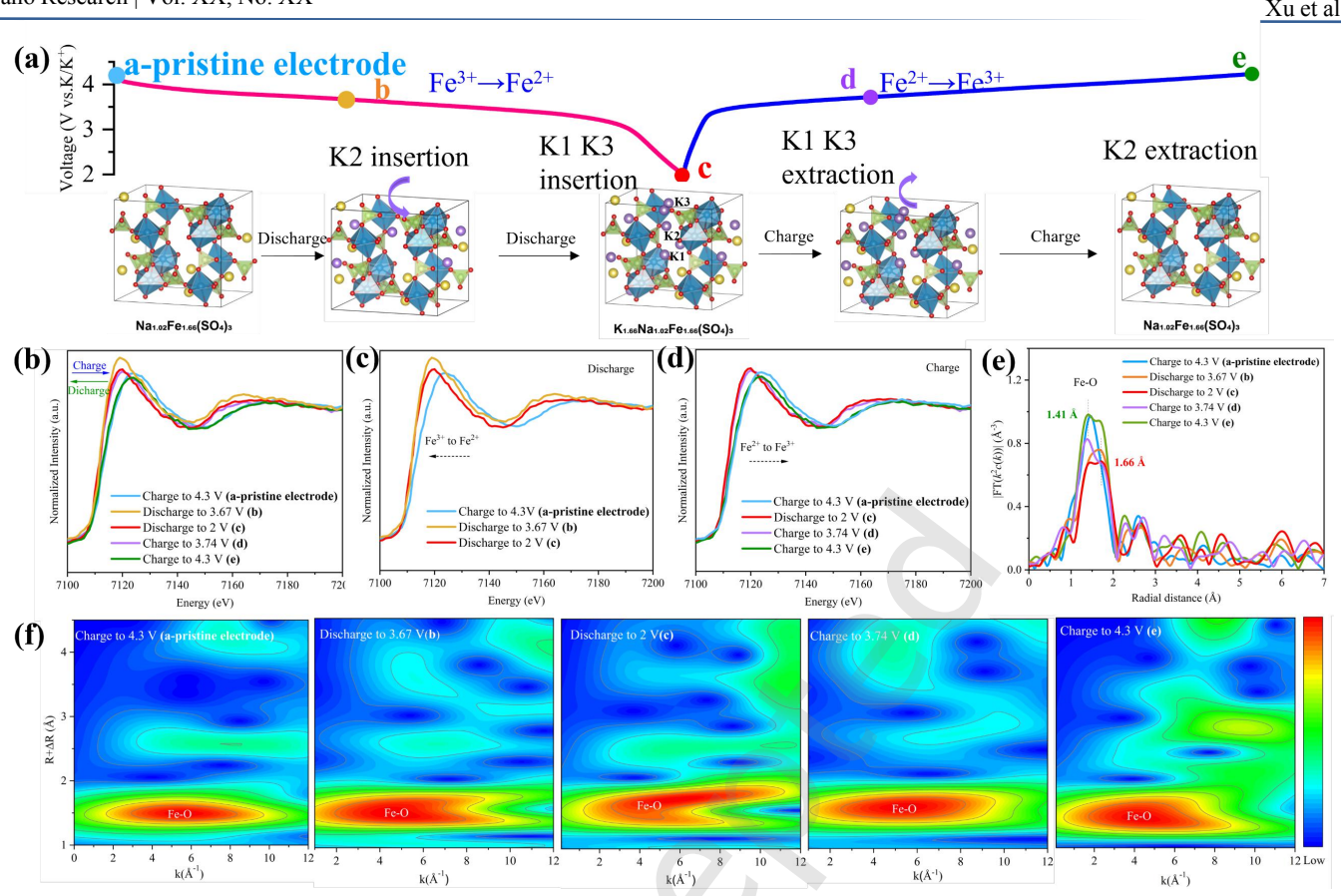


Figure 5. (a) Schematic diagram of crystal structure changes during charging/discharging of KNFS; (b) Fe K-edge absorption spectra during the charge/discharge process; (c) Fe K-edge absorption spectra at different SOC during the charging process; (d) Fe K-edge absorption spectra at different SOC during the discharging process; (e) Fourier-transformed extended EXAFS spectra in R-space at different SOC; (f) Wavelet transform patterns during the charge/discharge process.

To gain an in-depth understanding of the diffusion mechanism of K-ions in KNFS, this study employed density functional theory (DFT) calculations to investigate ion migration pathways within the three-dimensional framework (Figure 6a). Crystallographic analysis revealed three non-equivalent K sites in the unit cell. Through energyminimized migration trajectory calculations, the activation energies for key diffusion pathways were determined: the diffusion barriers for K1 to K1, K1 to K2, K2 to K3, and K3 to K3 were 0.521, 0.394, 0.393, and 0.743 eV, respectively (Figure 6b). All calculated diffusion barriers were below 1.0 eV, indicating relatively facile K-ion diffusion. Shorter migration distances and lower diffusion barriers enable

easier K-ion migration during charge/discharge processes, while multiple pathways accelerated K-ion transport rates, thereby enhancing the material's rate performance. The density of states (DOS) calculations for the KNFS sample were shown in Figure 6c. The DOS of KNFS exhibited a projected band gap of approximately 2.73 eV, which was significantly narrower than that of NFS (3.44 eV) reported in the literature [75]. The reduced energy gap between the conduction and valence bands indicated that spin-polarized electron transitions from the Fe 3d orbitals to the conduction band lowered the activation energy required for valence-toconduction band transitions. This mechanism significantly enhanced the material's electronic conductivity.

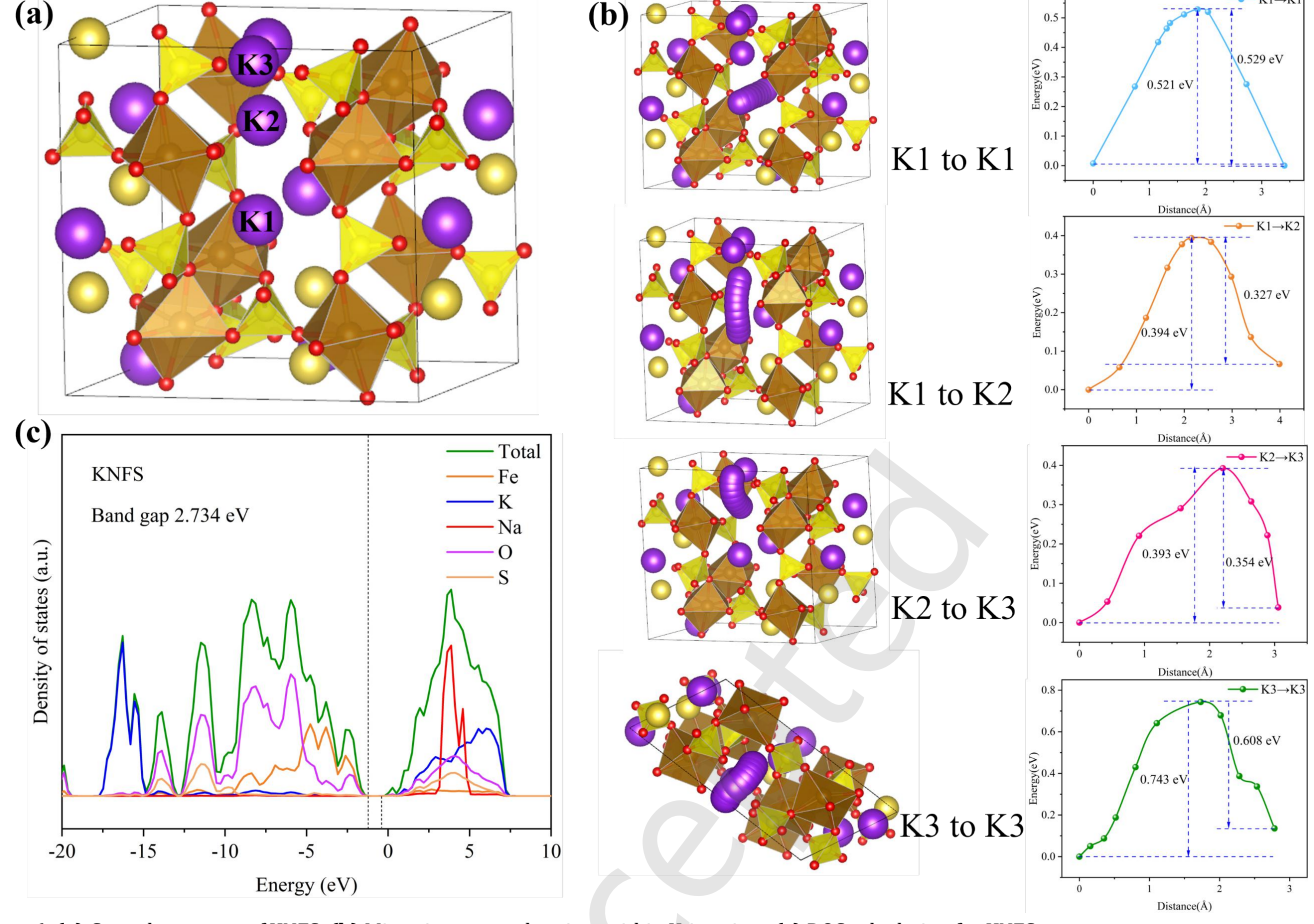


Figure 6. (a) Crystal structure of KNFS; (b) Migration energy barriers within K-ion sites; (c) DOS calculation for KNFS.

3 Conclusion

In summary, a novel KNFS material was synthesized using an electrochemical ion exchange method. The refined XRD result indicated that it possesses a typical alluaudite-type crystal structure with a lattice parameter of a = 13.1401 Å, b = 13.0138 Å and c = 6.5379 Å. As cathode material for PIBs, it delivered a reversible specific capacity of 83 mAh g⁻¹ at 0.1 C with a high average voltage of 3.84 V (vs. K/K+), and retained 88.2 % of its initial capacity after 300 cycles at 2 C. The insitu XRD and ex-situ XAFS analyses revealed that the KNFS cathode underwent reversible Fe³⁺/Fe²⁺ redox reactions, with its unit cell volume variation effectively limited to 2.57 %. The DFT and DOS calculations demonstrated that KNFS possessed multiple K-ion diffusion channels with low migration barriers, and exhibited a projected band gap of 2.73 eV. Owing to these characteristics, the KNFS system achieved a synergistic combination of high energy density (material-level: 319 Wh kg⁻¹), robust structural stability, and low cost, positioning it as a highly promising cathode candidate for large-scale energy storage applications. Furthermore, this work not only opens a new pathway for designing high-performance cathodes for PIBs but also provides a universal methodological reference for the development of materials in other alkali metal-ion battery systems.

4 Experimental section

4.1 Synthesis of NFS

All chemical reagents utilized in this investigation were of

analytical purity. The off-stoichiometry pure-phase alluaudite-type NFS synthesized via a spray-drying method combined with a solid-phase calcination process. First, 0.4 g of citric acid (C₆H₈O₇·H₂O₁, Sinopharm Chemical Reagents) was dissolved in 60 mL of deionized water under stirring for 2-3 minutes. The 5 g multi-walled carbon nanotube dispersion (MCNTs, Jiangsu Tiannai Technology Co., Ltd.) with a mass ratio of 5 wt.% MCNTs to deionized water was subjected to ultrasonic dispersion for 30 minutes. Subsequently, 5.68 g of sodium sulfate (Na₂SO₄, Sinopharm Chemical Reagents) was added and stirred for another 2-3 min until fully dissolved. Then, 13.9 g of ferrous sulphate (FeSO₄·7H₂O, Sinopharm Chemical Reagents) was directly introduced into the solution, followed by stirring for 3-5 min to ensure homogeneity. The solution was then transferred to a spray dryer operating at an inlet temperature of 105 °C and an outlet temperature of 60 °C, and the precursor was collected under continuous stirring throughout the spraydrying process. Finally, the precursor was calcined at 400 °C for 6 h with a temperature rise rate of 2 °C min⁻¹ under a (N_2) atmosphere to obtain the NFS@2%MCNTs composite material.

4.2 KNFS synthesis by electrochemical ion exchange

The NFS was assembled as the cathode using sodium metal as anode in SIBs and charged to 4.3 V to partially extract Naions from the NFS crystal structure. Subsequently, the battery was disassembled within a glovebox environment, and the desodiated electrode was thoroughly rinsed using a 1:1 (vol%) mixture of dimethyl carbonate (DMC) and ethylene carbonate (EC). This treated electrode was then

employed as the working electrode, paired with a potassium metal counter electrode. The electrochemical insertion of Kions into the crystal structure was achieved by discharging the cell to 2 V. KNFS was successfully synthesized by cycling the cathode material more than five times within a voltage window of 2.0–4.3 V (vs. K/K⁺). See **Figure S6** for details.

4.3 Materials Charactrization

The XRD (Bruker D8, Germany, Cu K α radiation, $\lambda = 1.5406$ Å, operating at 40 kV and 40 mA) was performed to characterize the crystallographic information and structural evolution of these cathode materials. The Generalized Structural Analysis System (GSAS-II) program was employed to refine the XRD data. A scanning electron microscope (SEM, JSM 7800 F, Japan) was used to investigate its morphological structure. The microscopic morphology and elemental composition of the material were characterized by transmission electron microscopy (TEM, ISM-2100F, Japan) and energy-dispersive X-ray spectroscopy (EDS). Fourier transform infrared (FT-IR, IR Prestige-21, USA) spectroscopy was used to examine the vibrational modes of functional groups in the wavenumber range of 400 to 1400 cm⁻¹. Raman spectroscopy (LabRam HR 800, USA) was performed to evaluate the graphitization degree of the coating carbon. Xray photoelectron spectroscopy (XPS, Thermo Scientific Kalpha, USA) was employed to determine the valence state of the element. The content of each elemental component was tested using ICP-OES (Thermo Fisher iCAP PRO, USA). In situ XRD experiment was carried out on Bruker D8 Advance diffractometer equipped with a Landt battery test system (CT-3002A, Wuhan, China), with a galvanostatic current of 10 mA g⁻¹. The Fe K-edge X-ray absorption spectra (XAS) were collected using a desktop X-ray absorption spectrometer (hiXAS, Germany), and all XAS data were processed with the Demeter analysis software. The migration pathways and energy barriers of K-ions were calculated using first-principles density functional theory (DFT), as implemented in the Vienna Ab initio Simulation Package (VASP, Austria).

4.4 Electrochemical tests

All electrochemical measurements were conducted at room temperature (25 °C). The CR-2016 coin-type potassium halfcells were fabricated in accordance with standard procedures. The cathode slurry was prepared by thoroughly mixing the active material, Super P conductive carbon black, and polyvinylidene fluoride (PVDF) binder that had been pre-dispersed in N-Methyl-2-pyrrolidone (NMP) solvent at a mass ratio of 8:1:1. The mixture was homogenized through planetary ball milling for 2 hours. The resulting slurry was uniformly coated onto an aluminum foil current collector via doctor-blade coating, followed by vacuum drying at 120 °C for 12 h to eliminate residual solvents. Circular electrodes (14 mm in diameter) with an active material areal loading of 5 ± 0.2 mg cm⁻² were precisely punched using a precision die-cutting machine. Cell assembly was conducted in an argon-filled glovebox (water and oxygen contents both < 0.01 ppm).

The NFS cathode, glass fiber separator (Whatman GF/C), and sodium metal foil anode were assembled together with 1 M NaPF $_6$ electrolyte dissolved in a mixture of ethylene

carbonate (EC) and propylene carbonate (PC) (1:1 v/v) containing 5 wt.% fluoroethylene carbonate (FEC) to construct the CR-2016 coin-type half-cells for SIBs. The KNFS cathode, glass fiber separator (Whatman GF/C), and potassium metal foil anode were assembled together with 0.8 M KPF₆ electrolyte dissolved in a mixture of ethylene carbonate (EC) and propylene carbonate (PC) (1:1 v/v) to construct the CR-2016 coin-type half-cells for PIBs. Electrochemical evaluations were conducted using a LAND CT2001A test system (Wuhan LAND Electric Co., Ltd., China) for galvanostatic charge/discharge testing and galvanostatic intermittent titration technique (GITT) measurements within a voltage range of 2.0-4.3 V (vs. K/K+). Cyclic voltammetry (CV) and electrochemical impedance spectroscopy (EIS) analyses were performed using a DH7006 electrochemical workstation (Jiangsu Donghua Testing Technology Co., Ltd., China).

Electronic Supplementary Material: Supplementary material (please provide the brief detail of the ESM) is available in the online version of this article at https://doi.org/10.26599/NR.2025.94908121.

Data availability

All data needed to support the conclusions in the paper are presented in the manuscript and/or the Electronic Supplementary Material. Additional data related to this paper may be requested from the corresponding author upon request."

Acknowledgements

This work was funded by the Science and Technology Commission of Shanghai Municipality (Grant No. 19D.Z.2271100), the China Postdoctoral Science Foundation (Grant No. 2024M750490). The authors would like to express their sincere gratitude to Ms. Li from Scientific Compass (www.shiyanjia.com) for her valuable assistance in XPS testing.

Declaration of competing interest

All the contributing authors report no conflict of interests in this work.

Author contribution statement

X. X. Y.: Data curation, validation, writing manuscript, experimental design. L. G. D.: validation, experimental design. Z. H.: Project administration, writing manuscript. W. N.: Project administration, Conceptualization. X. T. H.: Project administration, writing manuscript. Y. H.: Formal analysis. X. J.: Software. W. B. F.: Resources. Z. J. X.: Funding acquisition. L. Z. L.: Visualization, Supervision. C. Y. J.: Writing – review & editing. All the authors have approved the final manuscript.

Use of AI statement

None.

References

- [1] Tang, Y. W.; Liu, H. L.; Zhu, X.; Liu, M. T.; Tang, W. J.; Wei, G. X.; Feng, Y. H.; Xiao, B.; Wang, P. F. Restraining the Jahn–Teller Distortion in Mn-Based Layered Cathodes toward High-Performance Potassium-Ion Batteries. ACS Nano 2025, 19, 21118-21129.
- [2] Liu, Q.; Mu, Y. B.; Ye, T.; Lian, X. Y.; Su, Y. W.; Chen, X. P.; Shi, Z. X.; Meng, Z. X.; Zeng, L.; Sun, Z. T. et al. Transition Metal Atom–Cluster Synergistic Modification with Tuned d band Center Imparts Longevous Potassium Metal Anodes. *Angew. Chem. Int. Edit.* 2025, e202510150
- [3] Yang, X. H.; Yang, J. R.; Zheng, X. B.; Dou, Y. H.; Li, H. T.; Zhang, Y.; Li, Y. F.; Wang, D. S.; Yu, B.; Zhuang, Z. C. Enzyme Mimetic Single Atom Catalyst Design for Green Ammonia Synthesis. Adv. Energy Mater. 2025, 2501867.
- [4] Masese, T.; Yoshii, K.; Yamaguchi, Y.; Okumura, T.; Huang, Z. D.; Kato, M.; Kubota, K.; Furutani, J.; Orikasa, Y.; Senoh, H. et al. Rechargeable potassium-ion batteries with honeycomb-layered tellurates as high voltage cathodes and fast potassium-ion conductors. *Nat. Commun.* 2018, 9, 3823.
- [5] Zhang, W. C.; Huang, R.; Yan, X.; Tian, C.; Xiao, Y.; Lin, Z.; Dai, L. M.; Guo, Z. P.; Chai, L. Y. Carbon Electrode Materials for Advanced Potassium Ion Storage. *Angew. Chem. Int. Edit.* 2023, 62, e202308891.
- [6] Liu, G. P.; Sun, Z. P.; Shi, X. Y.; Wang, X. Y.; Shao, L. Y.; Liang, Y. H.; Lu, X. Y.; Liu, J. W.; Guo, Z. P. 2D Layer Structure Bi to Quasi 1D Structure NiBi₃: Structural Dimensionality Reduction to Superior Sodium and Potassium Ion Storage. Adv. Mater. 2023, 35, 2305551.
- [7] Zhao, S. Q.; Huang, Y.; Song, W. D.; Zhang, B. H.; Choi, Y.; Zhu, Z. Y.; Jiang, H. N.; Du, F.; Guo, S. J. High Entropy Tuning Enables Suppressed Phase Transition of Layered Manganese Based Oxides for High Mass Loading Potassium Ion Batteries. *Adv. Funct. Mater.* 2025, e11706
- [8] Jia, X. X.; Chen, H. Y.; Sun, H. T.; Zhu, J.; Lu, B. A. Promoting Robust Potassium Storage via Engineered Zn—S Bond. Adv. Energy Mater. 2025, 2501487.
- [9] Shi, J. D.; Cheng, Y. X.; Wang, T.; Peng, Y. H.; Lin, X. L.; Tang, B.; Feng, M. B.; Zhuang, Z. C.; Sun, Y. M.; Yu, X. et al. Site Specific Spin State Modulation in Spinel Oxides for Enhanced Nonradical Oxidation. *Angew. Chem. Int. Edit.* 2025, 64, e202504189.
- [10] Ren, P. F.; Gan, T.; Cai, J.; Hao, J. C.; Zhuang, Z. C.; Jin, C. Y.; Zhang, W. C.; Du, M. L.; Zhu, H. High Entropy Environments Enable Metal Surface Catalyzed Nucleophilic Electrooxidation. *Angew. Chem. Int. Edit.* 2025, 64, e202502776.
- [11] Meng, G.; Huang, Z. M.; Tao, L.; Zhuang, Z. C.; Zhang, Q. C.; Chen, Q. L.; Yang, H.; Zhao, H. P.; Ye, C. L.; Wang, Y. et al. Atomic Symbiotic Catalyst for Low Temperature Zinc Air Battery. *Angew. Chem. Int. Edit.* 2025, 64, e202501649.
- [12] Liu, T. C.; Yu, L.; Liu, J. J.; Lu, J.; Bi, X. X.; Dai, A.; Li, M.; Li, M. F.; Hu, Z. X.; Ma, L. et al. Understanding Co roles towards developing Cofree Ni-rich cathodes for rechargeable batteries. *Nat. Energy* 2021, 6, 277-286.
- [13] Lin, Y. C.; Luo, S. H.; Cong, J.; Shi, Z. Z.; Qian, L. X.; Yan, S. X.; Zhang, Y. H. Finding the perfect fit: Optimal Mn-ion site modification to improve the electrochemical performance of Ni/Co-free Mn-based layered oxide cathode toward potassium-ion batteries. *Chem. Eng. J.* 2025, 515, 163777.

- [14] Xu, J.; Kang, Q.; Peng, B.; Zhuang, Z. C.; Wang, D. S.; Ma, L. B. Engineering single-atom catalysts for sulfur electrochemistry in metal-sulfur batteries. *J. Energy Chem.* 2025, 106, 768-790.
- [15] You, X. C.; Guo, Z. Y.; Jiang, Q. L.; Xia, J. K.; Wang, S. W.; Yang, X. H.; Zhuang, Z. C.; Li, Y. F.; Xiang, H.; Li, H. et al. Magnetic-Field-Induced Spin Transition in Single-Atom Catalysts for Nitrate Electrolysis to Ammonia. *Nano Lett.* 2025, 25, 8704-8712.
- [16] Hou, X. H.; Kang, Q.; Huang, Y. H. Controlled hydrolysis of LiPF₆-based electrolytes with trace dual-unsaturated additives for high-temperature lithium-ion pouch batteries. *Nano Res.* 2024, 18, 94907475.
- [17] Tang, G. S.; Li, Y.; Wu, J. X.; Kang, Q.; Ma, L. B. Engineering heterostructured electrocatalysts for enhanced sulfur redox kinetics in metal–sulfur batteries. *Nano Research Energy* 2025, 4, 9120179.
- [18] Kang, Q.; Li, Y.; Zhuang, Z. C.; Yang, H. J.; Luo, L. X.; Xu, J.; Wang, J.; Guan, Q. H.; Zhu, H.; Zuo, Y. Z. et al. Engineering a Dynamic Solvent Phobic Liquid Electrolyte Interphase for Long Life Lithium Metal Batteries. Adv. Mater. 2024, 36, 2308799.
- [19] Hirsh, H. S.; Li, Y. X.; Tan, D. H. S.; Zhang, M. H.; Zhao, E. Y.; Meng, Y. S. Sodium Ion Batteries Paving the Way for Grid Energy Storage. Adv. Energy Mater. 2020, 10, 2001274.
- [20] Schmuch, R.; Wagner, R.; Hörpel, G.; Placke, T.; Winter, M. Performance and cost of materials for lithium-based rechargeable automotive batteries. *Nat. Energy* 2018, 3, 267-278.
- [21] Wang, X. Z.; Zuo, Y. T.; Qin, Y. B.; Zhu, X.; Xu, S. W.; Guo, Y. J.; Yan, T. R.; Zhang, L.; Gao, Z. B.; Yu, L. Z. et al. Fast Na⁺ Kinetics and Suppressed Voltage Hysteresis Enabled by a High Entropy Strategy for Sodium Oxide Cathodes. *Adv. Mater.* **2024**, *36*, 2312300.
- [22] Ma, X. M.; Zhang, D. W.; Fu, H. W.; Rao, A. M.; Zhou, J.; Fan, L.; Lu, B. A. Energy band-engineered solid electrolyte interphase for stable potassium-ion batteries. *Joule* 2025, 9, 101952.
- [23] Wu, L. C.; Dai, Z. Q.; Fu, H. W.; Shen, M K..; Cha, L. M.; Lin, Y.; Sun, F. F.; Rao, A. M.; Zhou, J.; Wen, S. C. et al. Multiple Electron Transfers Enable High Capacity Cathode Through Stable Anionic Redox. Adv. Mater. 2025, 37, 2416298.
- [24] Sha, M.; Liu, L.; Zhao, H. P.; Lei, Y. Review on Recent Advances of Cathode Materials for Potassium - ion Batteries. *Energy Environ. Mater.* 2020, 3, 56-66.
- [25] Yang, H.; Liu, Z. L.; Zhang, H.; Xu, X. Y.; Wu, W.; Wang, B. F.; Cao, Y. J.; Zhang, J. X. A low temperature iron-based phosphate potassiumion battery. *J. Power Sources* **2025**, *634*, 236494.
- [26] Zhao, L. K.; Zhou, J. L.; Gao, X. W.; Wang, X. C.; Bian, Y. H.; Liu, Z. M.; Gu, Q. F.; Luo, W. B. Antimony Trifluoride Engineered Hybrid Artificial Interphase Enable Dendrite Free Potassium Metal Batteries. Adv. Funct. Mater. 2025, 2502838.
- [27] Hwang, J. Y.; Kim, J.; Yu, T. Y.; Myung, S. T.; Sun, Y. K. Development of P3-K_{0.69}CrO₂ as an ultra-high-performance cathode material for K-ion batteries. *Energ. Environ. Sci.* 2018, 11, 2821-2827.
- [28] Liu, H. N.; Xu, J. Z.; Xu, Y. F.; Yuan, Z. Y.; Duan, L. P.; Lv, Y. Q.; Liao, J. Y.; Bao, J. C.; Zhou, X. S. Suppressing fluorine loss of KVPO₄F by surface chromium substitution for high-efficiency potassium-ion batteries. *Energy Storage Mater.* 2025, 75, 104017.
- [29] Zhang, Q.; Wang, Z. J.; Zhang, S. L.; Zhou, T. F.; Mao, J. F.; Guo, Z. P. Cathode Materials for Potassium-Ion Batteries: Current Status and Perspective. *Electrochem. Energy R.* 2018, 1, 625-658.
- [30] Zhang, W. C.; Liu, Y. J.; Guo, Z. P. Approaching high-performance potassium-ion batteries via advanced design strategies and engineering. *Sci. Adv. 5*, eaav7412.

- [31] Liu, Z. W.; Wang, Z. X.; Li, H. Y. Stabilization of the K_{0.43}V₂O₅ cathode by Ca ions substituted engineering strategy for high performance potassium ion batteries. *Chem. Eng. J.* **2025**, *514*, 163226.
- [32] Lin, B. W.; Zhu, X. H.; Fang, L. Z.; Liu, X. Y.; Li, S.; Zhai, T.; Xue, L.; Guo, Q. B.; Xu, J.; Xia, H. Birnessite Nanosheet Arrays with High K Content as a High Capacity and Ultrastable Cathode for K Ion Batteries. Adv. Mater. 2019, 31, 1900060.
- [33] Zhang, Z. Z.; Qiao, Y. R.; Heng, Y. L.; Liu, Y.; Kong, J. J.; Mao, M.; Jia, M. M.; Tang, H. W.; Wang, L.; Liu, D. H. et al. Durable Potassium Storage Achieved by Boron Coordination in a P2-Type Layered Oxide Skeleton. *Nano Lett.* 2025, 25, 6700-6707.
- [34] Xue, L. G.; Li, Y. T.; Gao, H. C.; Zhou, W. D.; Lü, X. J.; Kaveevivitchai, W.; Manthiram, A.; Goodenough, J. B. Low-Cost High-Energy Potassium Cathode. J. Am. Chem. Soc. 2017, 139, 2164-2167.
- [35] Guo, Q. B.; Han, S.; Lu, Y. X.; Xiao, R. J.; Li, J.; Hao, Q. L.; Rong, X. H.; Weng, S. T.; Niu, Y. S.; Ding, F. X. et al. Cation-self-shielding strategy promises high-voltage all-Prussian-blue-based aqueous K-ion batteries. *Nat. Commun.* 2025, 16, 4707.
- [36] Hu, Y.; Tang, W.; Yu, Q. H.; Wang, X. X.; Liu, W. Q.; Hu, J. H.; Fan, C. Novel Insoluble Organic Cathodes for Advanced Organic K Ion Batteries. Adv. Funct. Mater. 2020, 30, 2000675.
- [37] Gui, B. Y.; Yang, X. T.; Fu, H. W.; Peng, P.; Lyu, W.; Rao, A. M.; Zhou, J.; Fan, L.; Lu, B. A. Synergistic Electrode and Electrolyte Polarities Lead to Outstanding Organic Potassium - based Batteries. *Angew. Chem. Int. Edit.* 2025, 64, e202421928.
- [38] Park, W. B.; Han, S. C.; Park, C.; Hong, S. U.; Han, U.; Singh, S. P.; Jung, Y. H.; Ahn, D.; Sohn, K. S.; Pyo, M. KVP₂O₇ as a Robust High Energy Cathode for Potassium Ion Batteries: Pinpointed by a Full Screening of the Inorganic Registry under Specific Search Conditions. Adv. Energy Mater. 2018, 8, 1703099.
- [39] Huang, H. J.; Wu, X. W.; Gao, Y. J.; Li, Z. Y.; Wang, W.; Dong, W. S.; Song, Q. Y.; Gan, S. J.; Zhang, J. G.; Yu, Q. Y. Polyanionic Cathode Materials: A Comparison Between Na - Ion and K - Ion Batteries. Adv. Energy Mater. 2024, 14, 2304251.
- [40] Zhu, Y. X.; Ou, B. N.; Gao, C. W.; Gao, Y. T.; Zhang, B.; Kang, F. Y.; Zhai, D. Y. Ligand Engineering Enables Fast Kinetics of KVPO₄F Cathode for Potassium-Ion Batteries. ACS Energy Lett. 2024, 9, 3212-3218.
- [41] Li, Z.; Li, Z. C.; Zhang, Y. Z.; Yuan, X. Y.; Jin, H. B.; Zhao, Y. J. Enabling durable sodium storage of Fe-based fluorophosphate cathode via anion substitution. *J. Energy Chem.* 2025, 109, 850-858.
- [42] Li, Z. C.; Sun, C.; Wang, X. Y.; Li, Y.; Yuan, X. Y.; Jin, H. B.; Zhao, Y. J. Multi-element coupling driven high performance sodium-ion phosphate cathode. *Energy Storage Mater.* 2025, 76, 104141.
- [43] Gao, Y.; Zhang, H.; Liu, X. H.; Yang, Z.; He, X. X.; Li, L.; Qiao, Y.; Chou, S. L. Low - Cost Polyanion - Type Sulfate Cathode for Sodium - Ion Battery. Adv. Energy Mater. 2021, 11, 202101751.
- [44] Zhang, J. Y.; Yan, Y. L.; Wang, X.; Cui, Y. Y.; Zhang, Z. F.; Wang, S.; Xie, Z. K.; Yan, P. F.; Chen, W. H. Bridging multiscale interfaces for developing ionically conductive high-voltage iron sulfate-containing sodium-based battery positive electrodes. *Nat. Commun.* 2023, 14, 3701.
- [45] Zhao, A. L.; Ji, F. J.; Liu, C. Y.; Zhang, S. H.; Chen, K.; Chen, W. H.; Feng, X. M.; Zhong, F. P.; Ai, X. P.; Yang, H. X. et al. Revealing the structural chemistry in Na_{6-2x}Fe_x(SO₄)₃ (1.5 ≤ x ≤ 2.0) for low-cost and high-performance sodium-ion batteries. *Sci. Bull.* 2023, 68, 1894-1903.
- [46] Barpanda, P.; Oyama, G.; Nishimura, S. i.; Chung, S. C.; Yamada, A. A

- 3.8-V earth-abundant sodium battery electrode. *Nat. Commun.* **2014**, *5*, 4358.
- [47] Goñi, A.; Iturrondobeitia, A.; Gil de Muro, I.; Lezama, L.; Rojo, T. Na_{2.5}Fe_{1.75}(SO₄)₃/Ketjen/rGO: An advanced cathode composite for sodium ion batteries. *J. Power Sources* **2017**, *369*, 95-102.
- [48] Fang, Y. J.; Liu, Q.; Feng, X. M.; Chen, W. H.; Ai, X. P.; Wang, L. G.; Wang, L.; Ma, Z. Y.; Ren, Y.; Yang, H. X. et al. An advanced low-cost cathode composed of graphene-coated Na_{2.4}Fe_{1.8}(SO₄)₃ nanograins in a 3D graphene network for ultra-stable sodium storage. *J. Energy Chem.* 2021, 54, 564-570.
- [49] Liu, C. Y.; Chen, K.; Xiong, H. Q.; Zhao, A. L.; Zhang, H. Y.; Li, Q. Y.; Ai, X. P.; Yang, H. X.; Fang, Y. J.; Cao, Y. L. A novel Na₈Fe₅(SO₄)₉@rGO cathode material with high rate capability and ultra-long lifespan for low-cost sodium-ion batteries. eScience 2024, 4, 100186.
- [50] Lander, L.; Rousse, G.; Batuk, D.; Colin, C. V.; Dalla Corte, D. A.; Tarascon, J. M. Synthesis, Structure, and Electrochemical Properties of K-Based Sulfates K₂M₂(SO₄)₃ with M = Fe and Cu. *Inorg. Chem.* 2017, 56, 2013-2021.
- [51] Windhaus, M.; Mosel, B. D.; Müller-Warmuth, W. Mössbauer Studies of Fe²⁺ in Iron Langbeinites and other Crystals with Langbeinite Structure. 1998, 53, 27-37.
- [52] Hikita, T.; Itoh, K.; Okada, N.; Ohkubo, N.; Kodera, E. Mössbauer Spectroscopy of Langbeinite-Type K₂Fe₂(SO₄)₃. J. Phys. Soc. Jpn. 1996, 65, 1293-1296.
- [53] Driscoll, L. L.; Driscoll, E. H.; Slater, P. R. Investigation into the ability of langbeinite-type K₂M₂(SO₄)₃ (M = Mn, Fe, Co and Ni) materials to accommodate Na: The importance of the electronegativity of the framework cation. *J. Solid State Chem.* **2020**, *287*, 121363.
- [54] Park, H.; Kim, H.; Ko, W.; Jo, J. H.; Lee, Y.; Kang, J.; Park, I.; Myung, S. T.; Kim, J. Development of K₄Fe₃(PO₄)₂(P₂O₇) as a novel Fe-based cathode with high energy densities and excellent cyclability in rechargeable potassium batteries. *Energy Storage Mater.* 2020, 28, 47-54.
- [55] Shi, K. S.; Yang, W. S.; Wu, Q. D.; Yang, X. K.; Zhao, R. Y.; She, Z. Q.; Xie, Q.; Ruan, Y. J. Boosting the fast electrochemical kinetics of Na₄Fe₃(PO₄)₂(P₂O₇) via a 3D graphene network as a cathode material for potassium-ion batteries. *New J. Chem.* 2023, 47, 10153-10161.
- [56] Yang, W.; Liu, Q.; Yang, Q.; Lu, S. J.; He, W. X.; Li, L.; Chen, R. J.; Wu, F. Transitioning from anhydrous Stanfieldite-type Na₂Fe(SO₄)₂ Precursor to Alluaudite-type Na_{2+2δ}Fe_{2-δ}(SO₄)₃/C composite cathode: A pathway to cost-effective and all-climate sodium-ion batteries. *Energy Storage Mater.* 2025, 74, 103925.
- [57] Oyama, G.; Pecher, O.; Griffith, K. J.; Nishimura, S. i.; Pigliapochi, R.; Grey, C. P.; Yamada, A. Sodium Intercalation Mechanism of 3.8 V Class Alluaudite Sodium Iron Sulfate. *Chem. Mater.* 2016, 28, 5321-5328.
- [58] Xing, Z. Y.; Jian, Z. L.; Luo, W.; Qi, Y. T.; Bommier, C.; Chong, E. S.; Li, Z. F.; Hu, L. B.; Ji, X. L. A perylene anhydride crystal as a reversible electrode for K-ion batteries. *Energy Storage Mater.* 2016, 2, 63-68.
- [59] Han, J.; Li, G. N.; Liu, F.; Wang, M. Q.; Zhang, Y.; Hu, L. Y.; Dai, C. L.; Xu, M. W. Investigation of K₃V₂(PO₄)₃/C nanocomposites as high-potential cathode materials for potassium-ion batteries. *Chem. Commun.* 2017, 53, 1805-1808.
- [60] Hironaka, Y.; Kubota, K.; Komaba, S. P2- and P3-K_xCoO₂ as an electrochemical potassium intercalation host. *Chem. Commun.* **2017**, *53*,

3693-3696

- [61] Vaalma, C.; Giffin, G. A.; Buchholz, D.; Passerini, S. Non-Aqueous K-Ion Battery Based on Layered K_{0.3}MnO₂and Hard Carbon/Carbon Black. J. Electrochem. Soc. 2016, 163, A1295-A1299.
- [62] Liao, J. Y.; Hu, Q.; Mu, J. X.; He, X. D.; Wang, S.; Chen, C. H. A vanadium-based metal-organic phosphate framework material K₂[(VO)₂(HPO₄)₂(C₂O₄)] as a cathode for potassium-ion batteries. *Chem. Commun.* 2019, 55, 659-662.
- [63] Chihara, K.; Katogi, A.; Kubota, K.; Komaba, S. KVPO₄F and KVOPO₄ toward 4 volt-class potassium-ion batteries. *Chem. Commun.* 2017, 53, 5208-5211.
- [64] Pillai, S.; Dagadkhair, K.; Salame, P. H. Electrochemical and transport properties of nickel hexacyanoferrate (KNi[Fe(CN)₆]) as potential cathode material for aqueous potassium-ion batteries. *Chem. Phys. Lett.* 2024, 844, 141273.
- [65] Deng, T.; Fan, X. L.; Luo, C.; Chen, J.; Chen, L.; Hou, S.; Eidson, N.; Zhou, X. Q.; Wang, C. S. Self-Templated Formation of P2-type K_{0.6}CoO₂ Microspheres for High Reversible Potassium-Ion Batteries. *Nano Lett.* 2018, 18, 1522-1529.
- [66] Senthilkumar, B.; Selvan, R. K.; Barpanda, P. Potassium-ion intercalation in anti-NASICON-type iron molybdate Fe₂(MoO₄)₃. *Electrochem. Commun.* 2020, 110, 106617.
- [67] Naveen, N.; Park, W. B.; Han, S. C.; Singh, S. P.; Jung, Y. H.; Ahn, D.; Sohn, K. S.; Pyo, M. Reversible K⁺-Insertion/Deinsertion and Concomitant Na⁺-Redistribution in P'3-Na_{0.52}CrO₂ for High-Performance Potassium-Ion Battery Cathodes. *Chem. Mater.* 2018, 30, 2049-2057.
- [68] Wang, Y. Y.; Liu, J. H.; Du, P. H.; Sun, Z. L.; Sun, Q. Screening Topological Quantum Cathode Materials for K-Ion Batteries by Graph Neural Network and First-Principles Calculations. ACS Appl. Energy Mater. 2023, 6, 4503-4510.
- [69] Fedotov, S. S.; Luchinin, N. D.; Aksyonov, D. A.; Morozov, A. V.; Ryazantsev, S. V.; Gaboardi, M.; Plaisier, J. R.; Stevenson, K. J.; Abakumov, A. M.; Antipov, E. V. Titanium-based potassium-ion battery positive electrode with extraordinarily high redox potential. *Nat. Commun.* 2020, 11.
- [70] He, H. Y.; Xiao, J. C.; Zeng, S. H.; Li, Y. X.; Xie, J. J.; Chen, C. H. Construction of a bi-continuous charge transport network towards high-performance vanadium-based phosphate cathode materials for potassium ion batteries. *Nano Energy* 2024, 128, 109834.
- [71] Kim, H.; Seo, D. H.; Bianchini, M.; Clément, R. J.; Kim, H.; Kim, J. C.; Tian, Y.; Shi, T.; Yoon, W. S.; Ceder, G. A New Strategy for High - Voltage Cathodes for K - Ion Batteries: Stoichiometric KVPO4F. Adv. Energy Mater. 2018, 8.
- [72] Liao, J. Y.; Hu, Q.; Du, Y. C.; Li, J. B.; Duan, L. P.; Bao, J. C.; Zhou, X. S. Robust carbon nanotube-interwoven KFeSO₄F microspheres as reliable potassium cathodes. *Sci. Bull.* 2022, 67, 2208-2215.
- [73] Zhao, J.; Qin, Y. Y.; Li, L.; Wu, H.; Jia, X.; Zhu, X. L.; Zhao, H. Y.; Su, Y. Q.; Ding, S. J. Pillar strategy enhanced ion transport and structural stability toward ultra-stable KVPO₄F cathode for practical potassiumion batteries. *Sci. Bull.* 2023, 68, 593-602.
- [74] Liu, L. Y.; Liang, J. J.; Wang, W. L.; Han, C.; Xia, Q. B.; Ke, X.; Liu, J.; Gu, Q. F.; Shi, Z. C.; Chou, S. L. et al. A P3-Type K_{1/2}Mn_{5/6}Mg_{1/12}Ni_{1/12}O₂ Cathode Material for Potassium-Ion Batteries with High Structural Reversibility Secured by the Mg–Ni Pinning Effect. ACS Appl. Mater. Interfaces 2021, 13, 28369-28377.
- [75] Liu, C. Y.; Chen, K.; Li, F. M.; Zhao, A. L.; Chen, Z. X.; Fang, Y. J.;

- Cao, Y. L. Anion-doped Na_{2.9}Fe_{1.7}(SO₄)_{2.7}(PO₄)_{0.3} cathode with improved cyclability and air stability for low-cost sodium-ion batteries. *Nano Energy* **2024**, *125*.
- © The Author(s) 2025. Nano Research published by Tsinghua University Press. The articles published in this open access journal are distributed under the terms of the Creative Commons Attribution 4.0 International License (http://creativecommons.org/licenses/by/4.0/), which permits use, distribution and reproduction in any medium, provided the original work is properly cited.

Electronic Supplementary Material

A new iron-based sulfate cathode material for high-performance potassium-ion battery

Xinyue Xu¹, Guodong Li², Hao Zhang¹, Nan Wang², Tinghang Xu¹, Hui Yang¹, Jie Xu³, Baofeng Wang¹, Junxi Zhang¹ Zhaolu Liu¹.2 and Yongjie Cao 1.2 haolu Liu¹.2 and Yongjie Cao

Address correspondence to Yongjie Cao, yongjie_cao@fudan.edu.cn; Junxi Zhang, zhangjunxi@shiep.edu.cn; Zhaolu Liu, 24113010007@m.fudan.edu.cn

Supporting information to https://doi.org/10.26599/NR.2025.94908121

¹ Shanghai Key Laboratory of Materials Protection and Advanced Materials in Electric Power, Shanghai University of Electric Power, Shanghai 200090, China

² Department of Chemistry and Shanghai Key Laboratory of Molecular Catalysis and Innovative Materials, Fudan University, Shanghai 200433, China

³ School of Materials Science and Engineering, Anhui University of Technology, Ma'anshan 243002, China

Calculation process

1. Calcuation of reaction control proces

The determination of the reaction mechanism for KNFS was based on cyclic voltammetry (CV) measurements performed at various scanning rates, within a voltage window of 2.0–4.3 V and scanning rates ranging from 0.2 to 1 mV s⁻¹. This analysis was conducted using the following equation:

$$i = av^b$$
 (S1)
$$\log(i) = b \times \log(v) + \log(a)$$
 (S2)

Where "i" represents the peak current density, " υ " denotes the scanning rate, and "a" and "b" are associated parameters. A calculated "b" value of 1 indicates a surface-controlled capacitive process. Conversely, when the "b" value is approximately 0.5, it indicates a diffusion-controlled and battery-type reaction.

2. Computational analysis

All calculations were performed based on the DFT A $K_{10}N_{a6}Fe_{8}S_{12}O_{48}$ structure was built firstly. The PBE-GGA functional and PAW method are used with the energy cutoff of 520 eV [76]. The Van der Waals (vdW) interactions were considered using DFT-D3 method [77]. Spin polarization is considered. The structure is no longer relaxed when the energy convergence is less than 10^{-6} eV and the force at each atom is less than 0.01 eV/A.

3. Calculation of Energy Density and Power Density

The energy density and power density of the cathode in half cells were calculated based on the active mass of the cathode, as calculated using the following equation:

Energy Density (cathode) =
$$\frac{C(mAh) \times V \times 1000}{m_{\text{cathode}}}$$
 (S3)
Power Density (cathode) = $\frac{E}{t}$ (S4)

Herein, E is the energy density (Wh kg⁻¹), C is the discharge capacity of the battery (mAh), V is the average discharge voltage of the battery (V), m is the mass (kg) of KNFS; t is the discharge time (h).

4. Unit Cell Parameter Calculation

KNFS crystallizes in the C2/c space group, which adopts the monoclinic crystal system. The unit cell parameters of the monoclinic system comprise axis lengths a, b, and c, and interaxial angles $\alpha = 90^{\circ}$, $\beta \neq 90^{\circ}$, $\gamma = 90^{\circ}$. Consequently, full characterization requires determination of the parameters a, b, c, and β . The unit cell parameters were calculated using lattice spacing data extracted from the (020), (200), (131), and (002) diffraction planes according to the following equations:

$$\frac{1}{d_{hkl}^2} = \frac{h^2}{a^2 \sin^2 \beta} + \frac{k^2}{b^2} + \frac{l^2}{c^2 \sin^2 \beta} - \frac{2hl \cos \beta}{a \cos \ln^2 \beta}$$
 (S5)

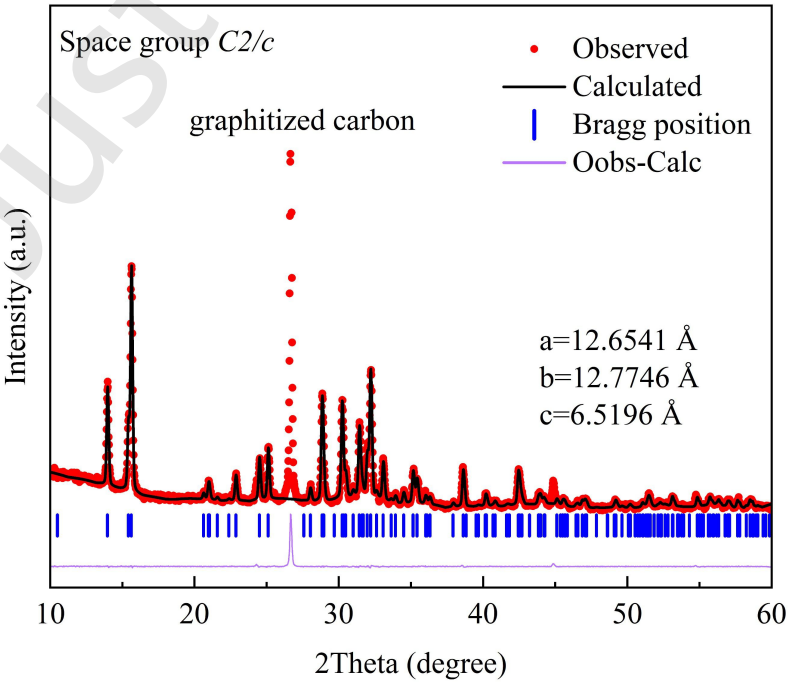


Figure S1. Rietveld refinement of the X-ray diffraction pattern for NFS.

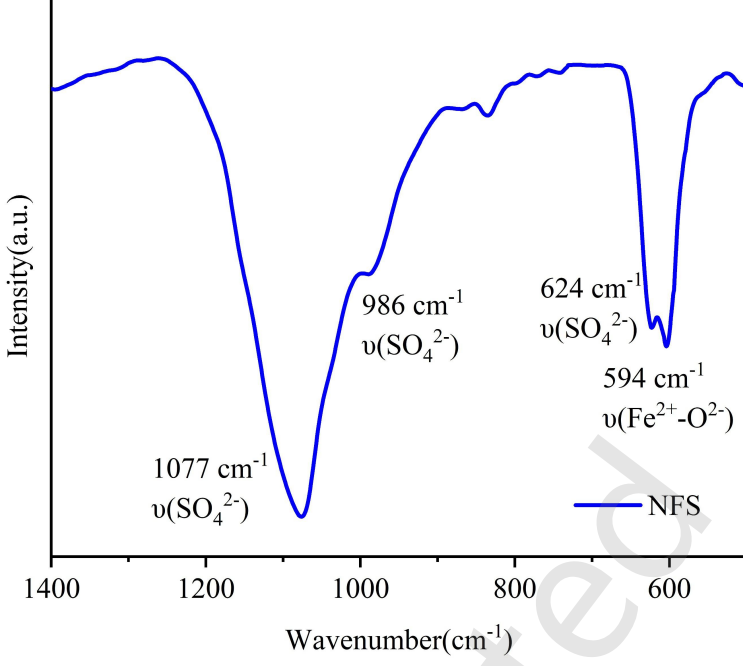


Figure S2. FTIR spectrum of NFS.

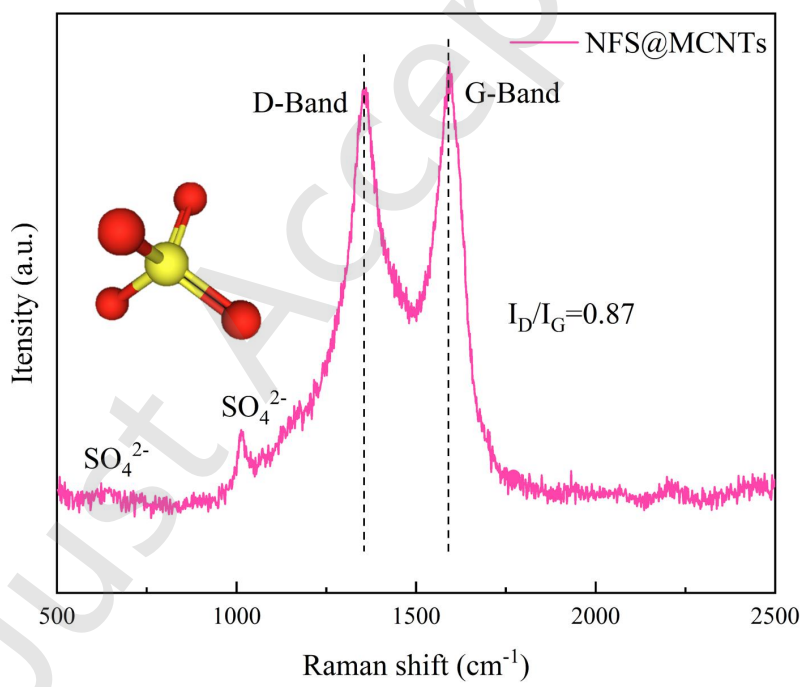


Figure S3. Raman spectrum of NFS@MCNTs.

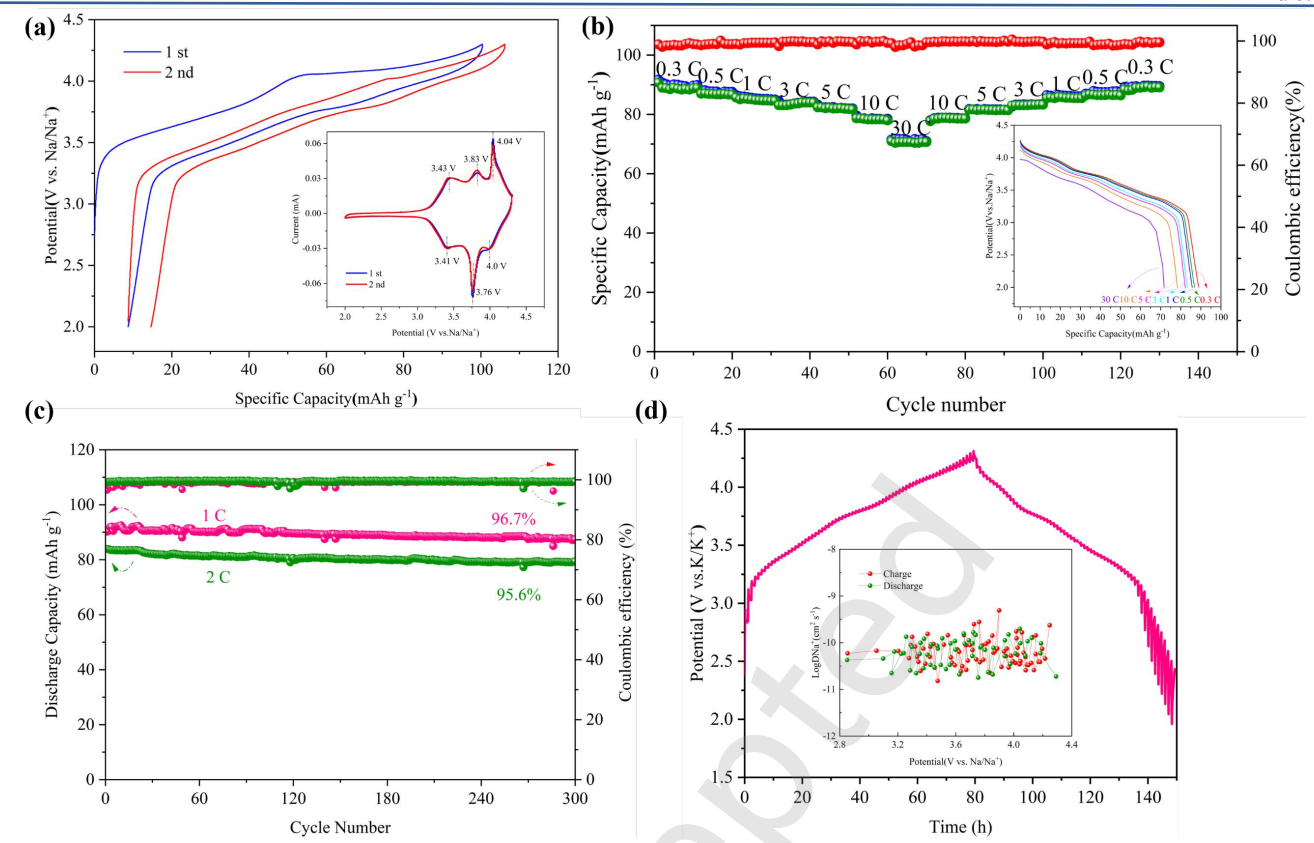


Figure S4. (a) Voltage profiles of NFS in the initial two cycles; The inset displays the corresponding CV curves; **(b)** Rate capability of the material and its discharge voltage profiles at various current rates; **(c)** Cycling stability of NFS at 1 C and 2 C; **(d)** GITT curves and Na-ions diffusion coefficients of of NFS.

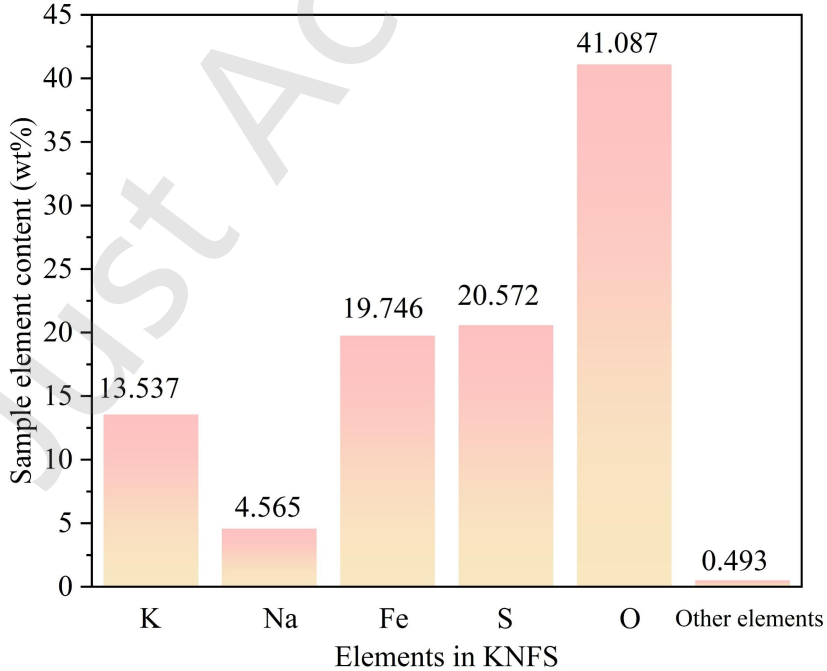


Figure S5. ICP graph of the elements in KNFS.

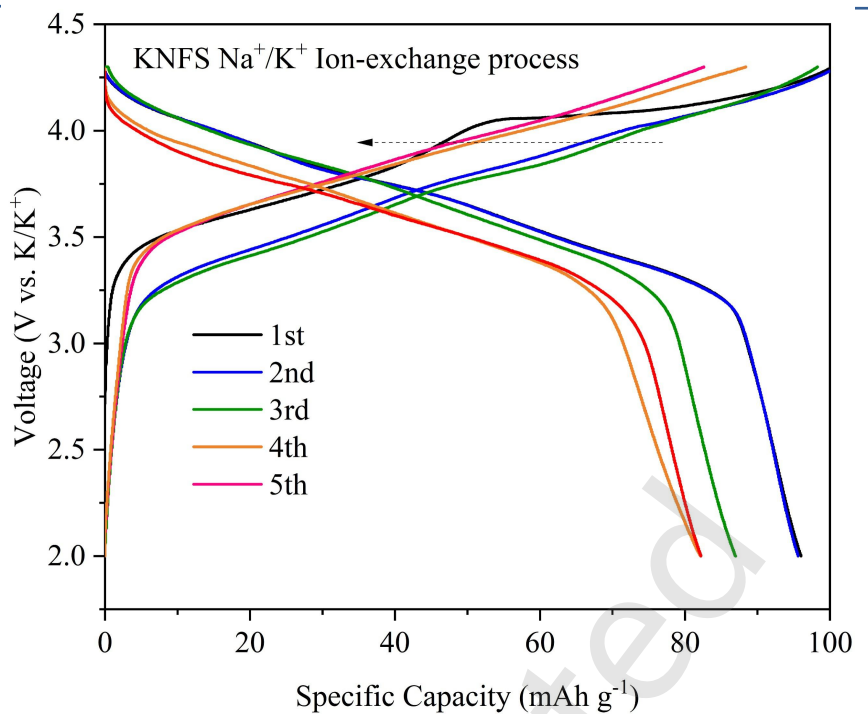


Figure S6. Electrochemical profiles of KNFS during Na⁺/K⁺ ion-exchange process for 5 cycles.

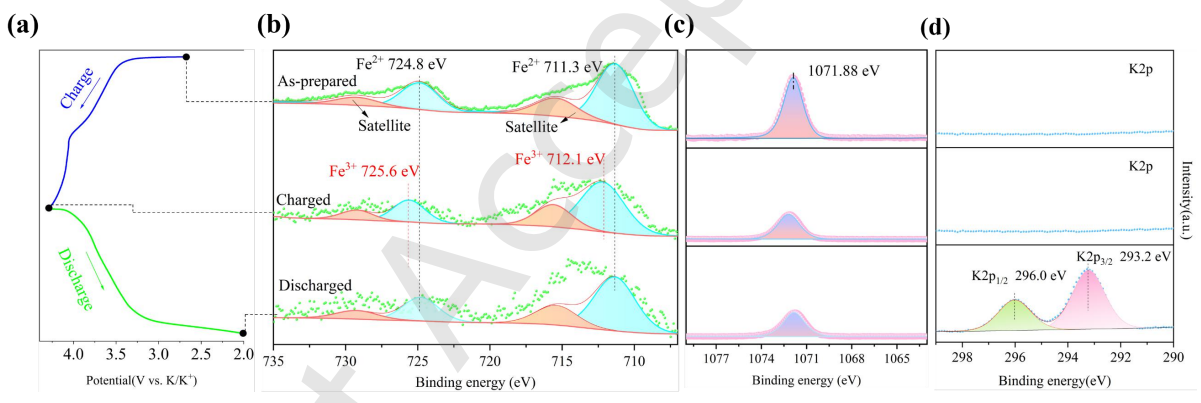


Figure S7. (a) Charge-discharge voltage profiles of the KNFS electrode; **(b)** *Ex situ* X-ray photoelectron spectroscopy (XPS) analysis of Fe 2p core-level spectra for the pristine KNFS electrode and those at charged (4.3 V) and discharged (2.0 V) states; **(c)** Na 1s and **(d)** K 2p spectra.

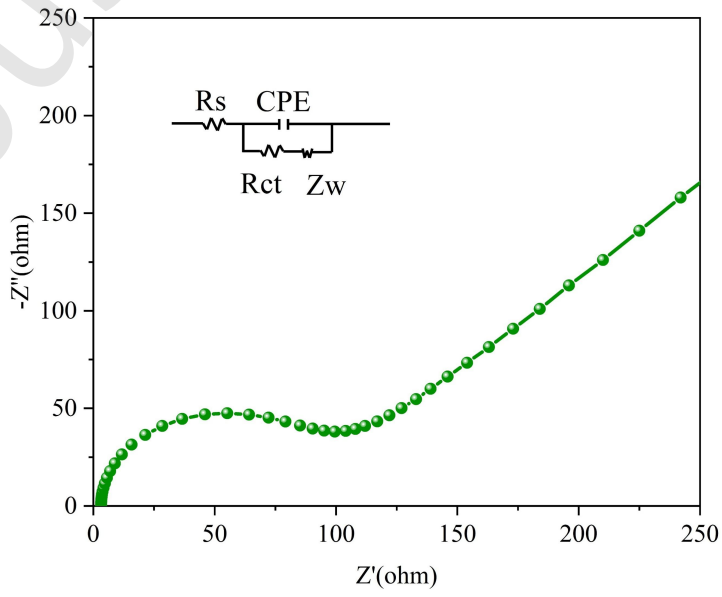


Figure S8. EIS analysis of the KNFS cathode in PIBs.

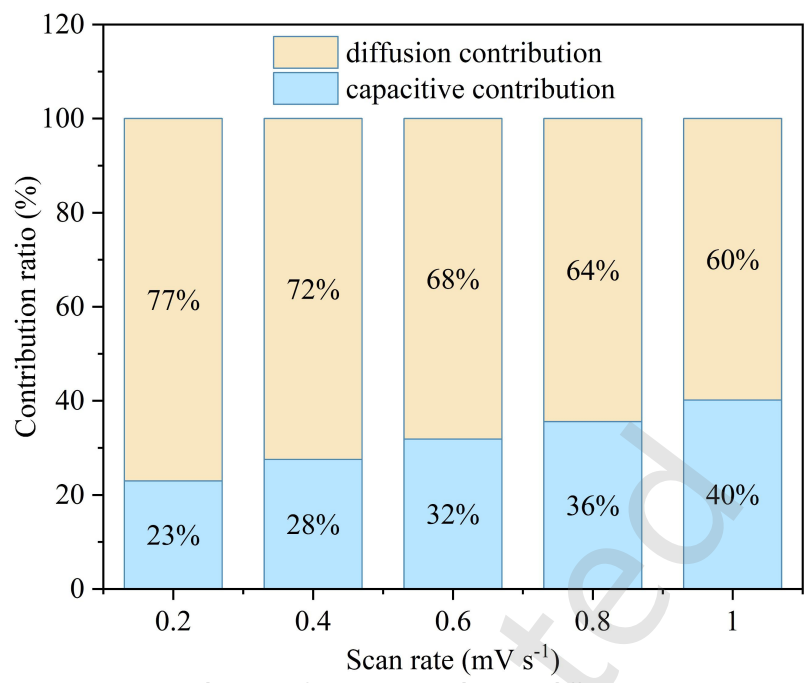


Figure S9. The ratios of capacitive contribution at different sweep rates.

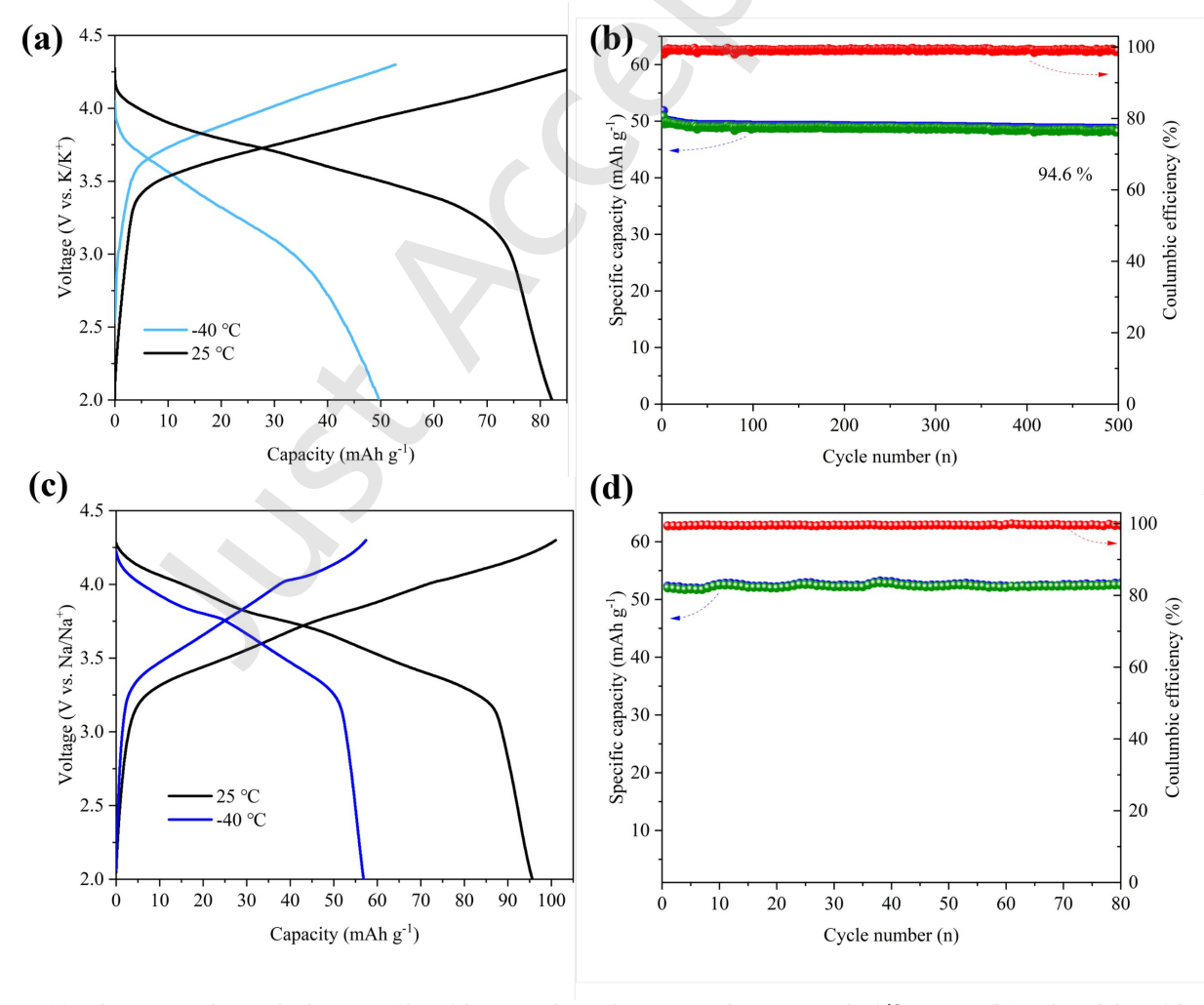


Figure S10. (a) Galvanostatic charge–discharge profiles of the KNFS electrode in PIBs under –40 °C and 25 °C at 0.1 C; (b) Cycle stability of the KNFS cathode in PIBs at 1 C; (c) Galvanostatic charge–discharge profiles of the NFS electrode in SIBs under –40 °C and 25 °C at 0.1 C; (d) Cycle stability of the NFS cathode in SIBs at 1 C.

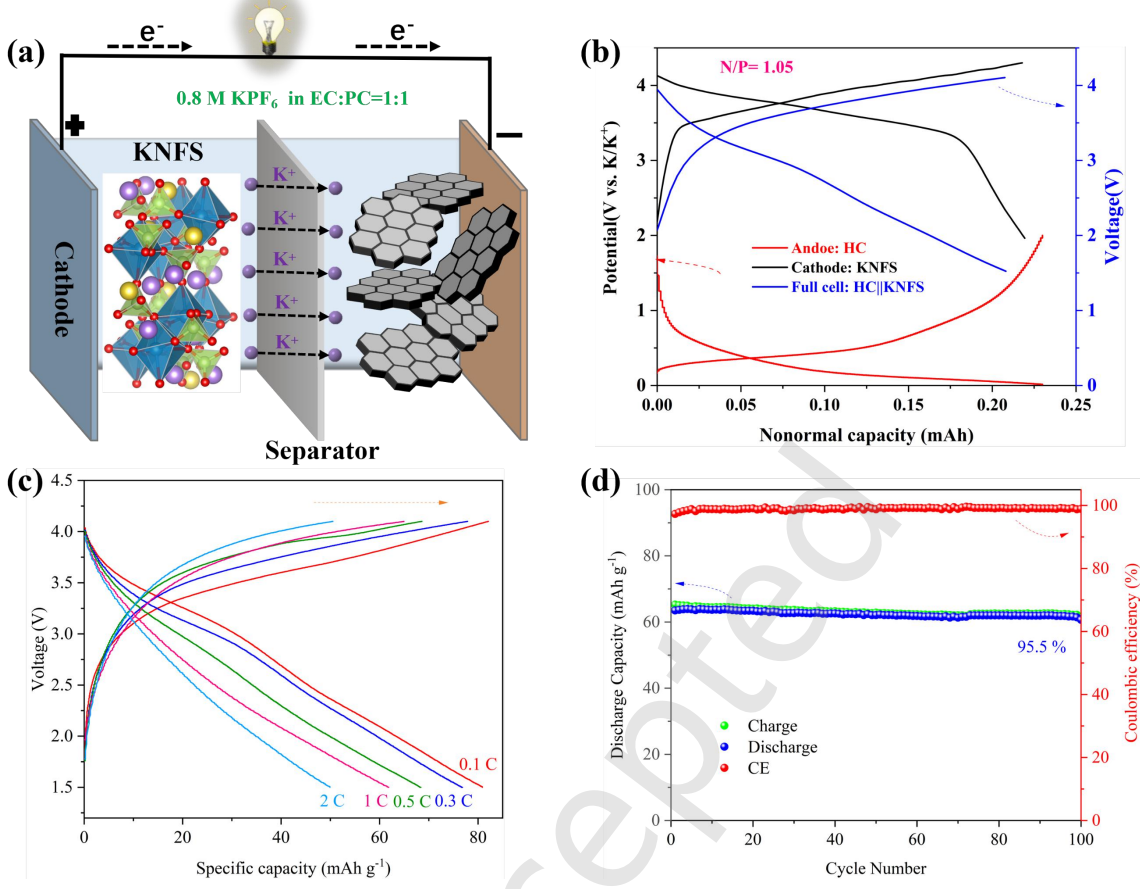


Figure S11. Electrochemical performance of the HC||KNFS full cell. **(a)** Schematic diagram of the full cell structure; **(b)** Charge/discharge curves of the HC anode, KNFS cathode, and the full cell; **(c)** Rate capability of the full cell at different current densities; **(d)** Cycling performance of the full cell at a current rate of 1 C.

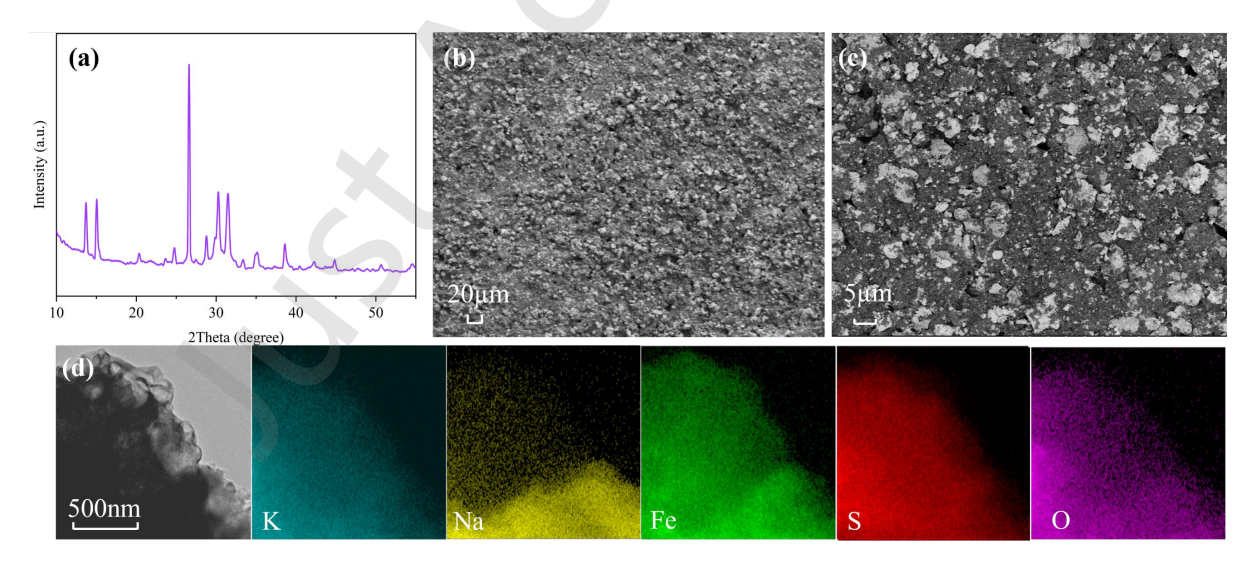


Figure S12. (a) XRD pattern of KNFS after 100 charge-discharge cycles at 2 C. **(b, c)** SEM images of the KNFS electrode at different magnifications. **(d)** Corresponding EDS elemental mapping after cycling.

Table S1. Crystallographic parameters of NFS and KNFS materials refined from powder XRD data at room temperature.

NFS	KNFS
C2/c (15)	C2/c (15)
12.654070	13.140130
12.774550	13.013820
6.519638	6.537853
951.02390	1008.44100
8.26288	7.78266
5.46427	5.64386
	C2/c (15) 12.654070 12.774550 6.519638 951.02390 8.26288

Table S2. Crystallographic parameters of NFS refined using the Rietveld method.

Atom	х	у	Z	
Na1	0.002000	0.013600	0.210000	
Fe1	0.268290	0.342850	0.352480	
S1	0.000000	0.274040	0.250000	
01	0.083900	0.343300	0.216000	
02	0.055200	0.207200	0.453000	
S2	0.240160	0.101970	0.131600	
03	0.236300	0.168900	0.316100	
04	0.181300	0.004300	0.124400	
05	0.323400	0.343800	0.082800	
06	0.360200	0.086600	0.169100	
Na3	0.000000	0.734900	0.250000	

Table S3. Crystallographic parameters of KNFS refined using the Rietveld method.

Atom	Х	у	Z	
Fe1	0.260433	0.332181	0.334161	
Na1	0.260433	0.332181	0.334161	
S1	0.000000	0.275940	0.250000	
01	0.085400	0.346200	0.219900	
02	0.053800	0.207860	0.454300	
S2	0.238910	0.102510	0.130900	
03	0.234000	0.170850	0.314600	
04	0.179400	0.003400	0.122800	
05	0.326000	0.341770	0.086100	
06	0.361000	0.086900	0.171700	
Na2	0.000000	0.734340	0.250000	
Na3	0.458988	0.041077	0.036531	
K1	0.000000	0.734340	0.250000	
K2	0.458988	0.041077	0.036531	
К3	0.006801	0.014301	0.217586	

Reference:

[76] Blöchl, P. E. Projector augmented-wave method. Phys. Rev. B 1994, 50, 17953-17979.

[77] Pereira, A. O.; Miranda, C. R. Atomic scale insights into ethanol oxidation on Pt, Pd and Au metallic nanofilms: A DFT with van der Waals interactions. *Appl. Surf. Sci.* **2014**, *288*, 564-571.